

**THE LYMAN-ALPHA FOREST AT $z \sim 4$:
KECK HIRES OBSERVATIONS OF Q 0000–26**

Limin Lu^{1,2}, Wallace L. W. Sargent¹, Donna S. Womble^{1,2}, & Masahide Takada-Hidai^{1,3}

(Accepted by the Astrophysical Journal)

¹ Palomar Observatory, California Institute of Technology, 105-24, Pasadena, CA 91125

² Hubble Fellow

³ On sabbatical leave from Research Institute of Civilization, Tokai University, Hiratsuka, Japan

ABSTRACT

We derive H I column density and Doppler width distributions for a sample of Ly α clouds with $3.4 < z < 4.0$, using a high resolution spectrum of the quasar Q 0000–26 ($z_{em} = 4.127$) obtained with the Keck telescope. Simulated Ly α forest spectra with matching characteristics are analyzed similarly in order to gauge the effects of line blending/blanketing and noise in the data. The H I column density distribution, after corrections for incompleteness resulting from line blanketing, is well described by a single power law function with index $\beta = -1.55 \pm 0.05$ over the column density range of $12.6 < \log N < 16.0$. A steepening in the column density distribution at $\log N(\text{H I}) > 14.5$ may be present. The Doppler width distribution of the clouds is consistent with a Gaussian function with a mean of 23 km s^{-1} and a dispersion of 8 km s^{-1} , but with a cutoff at 15 km s^{-1} , *ie*, no clouds with $b < 15 \text{ km s}^{-1}$ are required to describe the data. While the H I column density distribution found here is consistent with that derived from similar quality data at lower redshifts, both the mean Doppler width and the cutoff value are smaller than those found at lower redshift. There is a hint for clustering in the clouds' line of sight distribution in the velocity interval $100 < \Delta v < 160 \text{ km s}^{-1}$, but the evidence is only marginal. Analyses of the proximity effect indicate a value of $J_{\nu}^{LL} \sim 2 \times 10^{-22} \text{ erg s}^{-1} \text{ cm}^{-2} \text{ Hz}^{-1} \text{ sr}^{-1}$ for the mean intensity of the metagalactic UV ionizing background at $z \sim 4.1$, which is consistent with that expected from high-redshift quasars.

Subject heading: diffuse radiation - intergalactic medium - quasars: absorption lines - quasars: individual (Q 0000–26)

1 INTRODUCTION

Studies of Ly α absorption lines in spectra of quasars have seen rapid progress recently. On the one hand, the Hubble Space Telescope now allows for investigations of Ly α clouds over the important redshift region $z < 1.6$ (eg. Bahcall et al. 1993; 1996), while the advent of large aperture telescopes has greatly facilitated detailed observational studies of Ly α forest absorption at $z > 1.6$ at resolutions and S/N considerably higher than previously possible (eg. Hu et al. 1995; Tytler et al. 1995). On the other hand, advances in computing technology now allow for large-scale numerical simulations of structure formation in the early universe in various cosmological models. In particular, several recent papers (Cen et al. 1994; Petitjean, Mucket, & Kates 1995; Zhang, Anninos, & Norman 1995; Hernquist et al. 1996; Miralda-Escude et al. 1996) have explored the implications of these cosmological models for the nature of the Ly α absorption clouds. The results suggest that most Ly α clouds at high redshift ($2 < z < 4$) are likely associated with density enhancement in relatively low density regions of the universe in between collapsed structures. All these model calculations, with their different choices of cosmological parameters, different treatment of the physics involved, and different computational techniques, appear to reproduce the basic properties of Ly α clouds as inferred from observations. Thus more careful scrutiny of the models and more accurate knowledge of the Ly α cloud properties from observations are necessary in order to decide which cosmological model is correct.

In this paper, we present observations and analyses of the Ly α forest spectrum of the $z_{em} = 4.1$ quasar Q 0000–26 obtained with the Keck 10m telescope. The main aim is to derive accurate distributions of cloud parameters (redshift, H I column density, Doppler width), which can then be compared to similar distributions estimated for lower redshift clouds in order to study the evolution of the cloud properties. The study will also provide reliable observational reference against which theoretical models can be tested. Simulated Ly α forest spectra with matching characteristics to the observation are also analyzed in the same way in order to understand any biases that might exist in the derived parameter distributions resulting from line blending/blanketing, noise in the data, and the analysis technique itself.

The organization of the paper is as follows. After describing the observations and data reduction in §2, we discuss the profile fitting technique used to estimate z , $N(\text{H I})$, and Doppler b for the Ly α clouds (§3) and the numerical simulations (§4). The main observational results are presented in §5, including the distributions of column density

and Doppler width, the clustering property of the clouds along the line of sight, and a proximity effect analysis. The results obtained here are compared to results obtained in similar studies for lower redshift clouds and to recent theoretical models in §6. A summary of the main results is given in §7.

2 OBSERVATIONS AND DATA REDUCTION

We observed Q 0000–26 on 13 November 1993 with the High Resolution Echelle Spectrometer (HIRES) of the Keck 10m telescope (Vogt 1992). A 0.86" slit width was used to achieve a resolution of FWHM=6.6 km s⁻¹ with roughly 3 pixels per resolution element. Four exposures of 3000 sec each were obtained. Complete spectral coverage in the range of 5160-7580 Å was obtained with two partially overlapping setups. Data reductions were done in the usual manner using a software written by T. A. Barlow. After the echelle orders were extracted and wavelength- and flux-calibrated, they were resampled to a uniform wavelength scale (but keeping roughly the same number of pixels in a resolution element) and added together according to their S/N. The resulting spectrum has a typical S/N (per resolution element) in the Ly α forest region of 25-35:1, corresponding to a 4 σ detection limit of $N(\text{H I}) \sim 2.5 \times 10^{12} \text{ cm}^{-2}$ for an isolated Ly α line with a Doppler width $b = 20 \text{ km s}^{-1}$ (b is related to the velocity dispersion σ through the relation $b = \sqrt{2}\sigma$). The S/N longward of Ly α emission decreases from $\sim 80 : 1$ near the peak of the Ly α emission to 20-30:1 in the last echelle order covered.

The continuum level longward of the Ly α emission was established by fitting cubic splines to regions deemed free of absorption features using the IRAF task *continuum*. Such a procedure did not work very well in the Ly α forest region as most parts of the Ly α forest show no obvious continuum due to heavy absorption. We estimated the continuum level in the Ly α forest by picking out small “peaky” regions (typically a few Å wide) in the Ly α forest that are free of obvious absorption features and connecting them with straight lines. Some hand-editing of the continuum near the Ly α emission and the damped Ly α absorption at $z_{abs} = 3.39$ (see Figure 1) were necessary. The resulting continuum appears to describe the data satisfactorily. Figure 1 shows the Ly α forest portion of the HIRES spectrum along with the estimated continuum level. The continuum-normalized spectrum is shown in Figure 2 in finer detail, along with the 1 σ error spectrum. Note that the damped Ly α absorption at $z_{abs} = 3.39$ has already been removed from Figure 2. This damped Ly α absorption system will be analyzed elsewhere.

Absorption lines longward of the Ly α emission are selected using an automated software as described in Tripp, Lu, & Savage (1996), which yields a central wavelength, a measured equivalent width, and a 1σ error of the measured equivalent width for each absorption feature. In general, only features over the 4σ significance level are retained in the line list (Table 1). In a few cases, absorption features with significance level between 3 and 4σ that apparently correspond to lines in identified metal absorption systems are also retained and noted in the line list. We have attempted to identify all lines longward of the Ly α emission. These identifications are also given in Table 1. There are a number of weak ($< 6\sigma$) features which have no obvious identifications. We suspect most of these are C IV λ 1548 absorption lines whose corresponding weaker doublet members are below the 3σ significance level. Lines occurring in the Ly α forest that are associated with identified metal systems are also indicated in the line list. We did not attempt to identify new metal systems (eg, C IV doublets) based solely on lines in the Ly α forest as the probability for chance coincidence is expected to be very high. Based on the statistics of weak C IV systems: $dN/dz = 7.1$ for $w_r \geq 0.03 \text{ \AA}$ (Tripp et al. 1996), we expect roughly 4 C IV doublets with $w_r \geq 0.03 \text{ \AA}$ in the Ly α forest of Q 0000–26. Thus the level of contamination should be very small given that there are several hundred Ly α lines in the observed Ly α forest.

3 VOIGT PROFILE FITTING

At the resolution employed (FWHM=6.6 km s $^{-1}$), all Ly α lines are resolved. To derive the redshift, H I column density, and Doppler width for each individual Ly α cloud, we fit Voigt profiles to all Ly α lines between 5380 \AA and the Ly α emission. The lower cutoff of the fitting region is imposed by the damped Ly α absorption at $z_{abs} = 3.39$. Although we have a small coverage ($\sim 100 \text{ \AA}$) of the region below the Ly β emission line, where a number of Ly β absorption lines can be identified, we have decided not to use the Ly β lines to constrain the profile fitting in order to achieve uniform treatment of the entire line sample. In general, the Ly β lines are contaminated by Ly α forest lines at lower redshifts and their usefulness is limited.

The software we use to fit Voigt profiles is VPFIT developed by R. F. Carswell and collaborators and kindly made available to us. It is a χ^2 -minimization program which estimates simultaneously the redshift (z), column density (N or $N(\text{H I})$), Doppler width (b) and associated errors for each component (cloud) in the fitting region. At the high redshifts we are dealing with, most Ly α lines are more or less blended with neighboring

lines. Our fitting strategy is to divide the forest region into many sections where the two ends of each section recover to the continuum level, and to fit each section separately. The size of the sections ranges from a few angstroms in relatively uncrowded regions up to 50 Å in heavily blended regions, while the number of lines in the sections varies from a few to several tens. Clearly one needs a convenient, meaningful, and objective way to decide how many components to insert in fitting a section. We start with the minimum number of lines (components) recognizable to the eye, and add more lines as needed until a reduced χ^2 of ≤ 1.1 per degree of freedom is achieved. Occasionally this “rule” has to be relaxed in order to accommodate spectral regions where cosmic ray events or defects on the detector not removable by the flatfielding procedure have apparently corrupted the spectrum (eg, regions around 5595, 5867, and 5955 Å). We also examine the residuals of the fits and find that the above stopping criterion almost always yields visually appealing results (see figure 2).

Identified metal lines in the Ly α forest are also fitted using similar procedures in order to recover any Ly α lines blended with the metal absorption lines. Lines from the same ion species (eg, Si IV $\lambda\lambda$ 1393, 1402) in a given system are fitted simultaneously with their parameters tied together.

The final list of Ly α and metal lines resulting from the Voigt profile fitting process is given in Table 1, where we give a line number for identification, central wavelength of the absorption, identification, redshift, column density, and Doppler width, along with the 1σ errors where appropriate. The VPFIT results are also shown in Figure 2 superimposed on the observed spectrum. Only the Ly α lines will be discussed in the remainder of this paper. The metal systems will be discussed in a future paper when combined with spectra of other quasars.

4 NUMERICAL SIMULATIONS

Most weak Ly α lines are expected to be lost in the observed spectrum due to heavy line blanketing. In order to derive unbiased distributions of column density and Doppler width, we generate simulated Ly α forest spectra from computer codes and fit the simulated spectra in the same way as we do for the observed spectrum. This procedure should help us to understand and, in some cases, to correct for effects that are caused by line blending/blanketing and/or the Voigt profile fitting process itself.

The simulated spectra have the same spectral coverage, resolution, sampling rate (pixel size), and S/N as the observed one. Ly α lines are drawn randomly from given distributions in z , N , and b . The assumed distribution is:

$$f(z, N, b) = A(1 + z)^\gamma N^{-\beta} e^{-\left(\frac{b-b}{\sqrt{2}\sigma}\right)^2} \quad (1)$$

for $N_{min} \leq N \leq N_{max}$ and $b_{cut} \leq b \leq b_{max}$. This functional form has been found to give reasonable descriptions of the observed properties of Ly α clouds (cf. Carswell 1988). In order for the simulations to be as realistic as possible, all metal lines that occur in the observed Ly α forest of Q 0000–26 (including those which are expected to occur in the Ly α forest but are not recognizable in the observed spectrum because of blanketing) are inserted back into the simulated spectra using the parameters derived from VPFIT (section 3 above). A proximity effect (cf. Bajtlik, Duncan, & Ostriker 1988; see also §5.5) is also put in the simulation using the parameters given in §5.5. The normalization constant in equation (1) is adjusted such that the resulting simulated spectra have the same mean D_A value (=0.511 between [5400, 6100] Å) as the observed spectrum (see §5.5 for an explanation of D_A).

We fix the value of γ at 2.75 (Lu, Wolfe, & Turnshek 1991). For the small redshift range considered here, the exact value of γ is not important. We also choose $b_{max} = 100$ km s $^{-1}$ based on the results of previous studies (cf. Carswell 1988), and set $N_{max} = 10^{18}$ cm $^{-2}$ in order to avoid damped Ly α absorption lines. The remaining parameters in equation (1) (β , N_{min} , $\langle b \rangle$, σ , and b_{cut}) are then varied in order to explore the parameter space. The resulting simulated spectra are subjected to several simple tests to select out the “best candidates” for profile fitting and for further comparison with the observed spectrum. In the first test, we compare the intensity distribution of the pixels between the simulated spectra and the observed spectrum in the spectral region [5400, 6100] Å. In the second test, we compare the power spectrum of the simulated spectra and the observed spectrum in the same spectral region. The first test appears to be reasonably sensitive to the column density distribution, while the second test appears to be more sensitive to the Doppler width distribution. After this preliminary screening, simulations which compare favorably with the observed spectrum are fitted with Voigt profiles using the same procedure as described in §3, and the results are compared with those from fitting the observed spectrum. The parameters that match the observation the best are given in Table 2. In the remaining discussion, unless noted otherwise, the results of profile fitting one arbitrary simulated

spectrum using the parameters given in Table 2 will be compared to the results of profile fitting the observed Q 0000–26 spectrum.

5 RESULTS

$\text{Ly}\alpha$ lines near quasar emission redshifts are affected by the proximity effect (cf. Bajtlik et al. 1988), and they should not be used in deriving unbiased distributions of cloud parameters. Thus we define *Sample 1* as all $\text{Ly}\alpha$ clouds within the redshift range $3.425543 \leq z \leq 3.976680$, corresponding to the wavelength range $5380 \leq \lambda \leq 6050$. The upper cutoff at 6050 Å is chosen because this is where the UV ionizing intensity from the quasar is expected to roughly equal that of the UV background (section 5.5). There are 336 $\text{Ly}\alpha$ lines in Sample 1 for the real data, and 373 lines for the simulation. The mean redshift of the sample is $\langle z \rangle = 3.7$.

For some purposes, it is useful to have a sample where the measurements of cloud parameters from VPFIT are relatively well determined so that scatters due to noise/blending would be small. Thus we define *Sample 2* as a subsample of Sample 1 with measurement uncertainties $\sigma_{\log N} \leq 0.1$ and $\sigma_b \leq 5 \text{ km s}^{-1}$ from profile fitting. Sample 2 contains 227 lines for the real data and 235 lines for the simulation. Note that none of the $\text{Ly}\alpha$ lines with $N > 10^{16}$ from the profile fitting is retained in Sample 2. These lines are strongly saturated and their measured parameters from VPFIT are extremely uncertain.

It is worth pointing out that $\text{Ly}\alpha$ lines associated with identified metal systems are included in the above samples if they satisfy the selection criteria. While traditionally the metal systems and $\text{Ly}\alpha$ clouds which do not show obvious metal absorption have been treated differently since they may belong to different parent populations (cf. Sargent et al. 1980), recent studies suggest that they may in fact be related. For example, Lu (1991) showed using a composite spectrum that many of the previously-thought-metal-free $\text{Ly}\alpha$ clouds actually contain metals. This is corroborated by recent high quality Keck observations (Cowie et al. 1995; Tytler et al. 1995; Sargent et al. 1996). In particular, these authors concluded that roughly half of the $\text{Ly}\alpha$ clouds with $3 \times 10^{14} < N(\text{H I}) < 10^{15} \text{ cm}^{-2}$ show C IV absorption, while essentially all $\text{Ly}\alpha$ clouds with $N(\text{H I}) > 10^{15} \text{ cm}^{-2}$ show C IV absorption. The limiting $N(\text{H I})$ above which $\text{Ly}\alpha$ clouds are found to show detectable metal absorption is still limited by the sensitivity of the data. Hence, in principle, all $\text{Ly}\alpha$ clouds *could* contain metals. Additionally, some authors (cf. Cristiani et al. 1995) have found evidence for clustering in the “traditional” $\text{Ly}\alpha$ forest clouds, further blurring

the differences between metal systems and the “traditional” Ly α forest clouds. We will therefore not make the distinction between metal systems and Ly α forest clouds *with respect to the Ly α absorption* for the purpose of this work. It is important to note that this choice makes little difference to the statistical results as the number of identified metal systems is very small compared to the number of forest clouds.

5.1 Column Density - Doppler Width Relation

In Figure 3 we plot b vs $\log N$ for Ly α clouds in Sample 1 for Q0000–26 and for an arbitrary simulation using the parameters given in Table 2 for which we have performed profile fitting. Figure 4 shows the equivalent for Sample 2, but with error bars.

There are a number of interesting features in the N - b distribution that are worth mentioning. First, we note the remarkable similarity between the simulation and the actual data. Secondly, we note the voids in the upper-left corner of the $N - b$ distribution for both the real data and the simulation. Since the input cloud distribution to the simulation contains many clouds in this region, the aforementioned void apparently results from line blending and the limited S/N of the data: these lines are wide and shallow and thus are easier to miss. We also note another artifact in the N - b distribution: the presence of very narrow ($b < 15 \text{ km s}^{-1}$) lines, especially at low column densities. These narrow clouds are not present in the input distribution to the simulation, and they are clearly a manifestation of line blending and noise in the data. Similar conclusions have been reached by Rauch et al. (1992, 1993). The number of these very narrow lines drops dramatically in Sample 2 (Figure 4), suggesting that higher S/N should reduce this bias. Even though at face value Figures 3 & 4 may suggest significant correlations between N and b , the simulation results indicate that such apparent correlations are probably artifacts due to line blending and insufficient S/N. Thus the real cloud distribution is consistent with no intrinsic correlation between N and b . On the other hand, if indeed there is an intrinsic lack of Ly α clouds with low- N and high- b in nature, such an effect will be difficult to recognize for the reasons described above.

We also note the relative lack of clouds with $b < 15 \text{ km s}^{-1}$ in the real data, which is most obvious in Figure 4 where the scatter due to noise and blending is smaller. The agreement in the b cutoff between the real data and the simulation, whose input cloud distribution has a cutoff at $b_{cut} = 15 \text{ km s}^{-1}$, suggests that the observed cloud distribution is consistent with having no clouds with $b < 15 \text{ km s}^{-1}$. The few clouds seen with $b < 15$

in the real data are probably either due to noise/blending or are unidentified metal lines (most likely single members of the C IV doublets with the other member blended with other lines). Since we can successfully recover narrow metal lines put in the simulations (see also Table 1), *the lack of very narrow Ly α lines in the Q 0000–26 spectrum is not an artifact of the profile fitting process.*

To further test the reality and accuracy of the cutoff b value, figure 5 shows the N - b relation for another simulation where the input cloud distribution has a $b_{cut} = 18 \text{ km s}^{-1}$. One can see that the recovered cloud distribution from VPFIT shows much better agreement with a cutoff b value of 18 km s^{-1} than with a cutoff value of 15 km s^{-1} . Hence we believe the cutoff b value of 15 km s^{-1} estimated for the real data is fairly robust.

There is some evidence that the b cutoff increases slightly with H I column density, as suggested in Hu et al. (1995). Interestingly, such a dependence of b_{cut} on column density appears to have a possible physical origin as demonstrated by the CDM simulations of Zhang et al. (1995, see their figure 4). This dependence arises because higher column density clouds appear to be associated with denser regions where the gas is hotter due to the increasing shock velocities (Miralda-Escude et al. 1996). A similar dependence of b_{cut} on $N(\text{H I})$ is visible in our data for Q 0000–26 (Figures 3 & 4, upper panels). However, we see the same dependence in some of our simulations (cf. Figure 5), which suggests that this dependence of b_{cut} with column density can also be created by the profile analysis procedure itself. Thus we are not confident of the reality of this dependence.

5.2 Column Density Distribution

In the upper panel of Figure 6 we show the column density distribution from Sample 1. The solid histogram is for the observation, and the dotted histogram is for the simulation. The dashed straight line illustrates the input distribution to the simulation, which has an index of $\beta = 1.53$. We first note the good agreement between the distributions from the simulation and from the observation, which is taken as an indication that the simulation parameters must be substantially correct. We also note the progressively larger discrepancy toward lower column density between the input cloud distribution and that recovered from VPFIT to the simulated spectrum. This is apparently due to the line blanketing effect since the simulated spectrum has enough S/N to detect most of these “missing” lines if they are isolated. We have used the simulation to correct for the incompleteness of the observed distribution, and the resulting distribution is shown in the lower panel of Figure

6. However, the corrections are only made for the data points at $\log N < 13.5$ because the distribution at $\log N > 13.5$ appears to be largely unaffected by the line blanketing effect (in the statistical sense), and because the bins at higher column densities contain fewer lines and the correction factors are more uncertain. A χ^2 fit to the corrected $N(\text{H I})$ distribution yields $\beta = 1.55 \pm 0.05$ for $12.6 \leq \log N \leq 16.0$. The lowest column density bin was not used in the fit because the correction factor is very large (~ 25) and relatively uncertain (this bin is near the detection limit for the quality of our data). We also tried different correction regions and fitting regions. These results are summarized in Table 3. Evidently all fits given in Table 3 are acceptable.

We note that Hu et al. (1995) obtained $\beta = -1.46$ with a 95% confidence range of $(-1.37, -1.51)$ in the column density range $12.3 \leq \lg N \leq 14.5$ based on the analysis of similar Keck data, but at a mean redshift of 2.8. We obtain $\beta = 1.46 \pm 0.06$ for the same column density range, in excellent agreement with the Hu et al. determination.

It has been suggested that there may be a steepening in the column density distribution of Ly α clouds at $\log N > 14$ (Carswell et al. 1987; Giallongo et al. 1996). Similarly, both Petitjean et al. (1993) and Hu et al. (1995) demonstrated that there is a deficit of clouds in the column density range $14.5 < \log N < 17$ compared to a power-law extrapolation of the distribution from lower column densities. The physical cause of this deficit is not exactly clear. We see a hint of such a deficit in our data (Figure 6), although the deficit is not very significant since a single power law function yields an acceptable fit to the distribution over the entire column density range $12.6 < \log N < 16.0$.

5.3 Doppler Width Distribution

In Figure 7 we show the distribution of Doppler parameters for lines in Sample 1 and Sample 2 for both the observation and the simulation. We also show with the smooth dotted curves the input b distribution to the simulation. It is seen that the observation and the simulation yield very similar Doppler width distributions. A Kolmogorov-Smirnov test indicates that the observed b distribution is consistent with that from the simulation: the probabilities for the two distributions to be drawn from the same parent population are 16% and 49% for Sample 1 and Sample 2, respectively.

As discussed in §5.1, the combination of noise and blending has created several artifacts. The first of which is the “creation” of clouds with very small b values ($< 15 \text{ km s}^{-1}$) at low column densities. This effect can be remedied with higher S/N observations.

The second is the “creation” of excessive clouds with large b values over the input distribution (figure 7), some as large as 100-200 km s⁻¹ (see figure 3). A careful examination of the clouds with estimated $b > 100$ km s⁻¹ indicates that they are always associated with region of the spectrum where blending from a multitude of lines have pulled the entire spectrum below the continuum. Thus these broad features are chiefly caused by heavily blended forest lines. Imperfect placement of the continuum level in the observed spectrum may also play a role, although its effect is difficult to assess. In any case, the fact that the Doppler width distributions from the real data and from the simulation agree well suggests that the input Doppler distribution given in equation (1) and Table 2 is a reasonably good description of the real distribution.

Tytler et al. (1995) suggested that there are several types of Ly α lines, including a type of very narrow lines ($b \sim 3 - 15$ km s⁻¹) and a type of very shallow, broad lines ($b \sim 60 - 200$ km s⁻¹). The data used in the Tytler et al. study are of similar resolution as ours but with ~ 3 times better S/N. The existence of such narrow lines would imply very cool clouds with temperature significantly below the canonical value of a few $\times 10^4$ K. The existence of the very broad lines might suggest hot, collisionally ionized gas, which could contain lots of baryon. However, our simulation results indicate that such very narrow and very broad features could be introduced artificially by noise and blending. Although we suspect that at least some of the very narrow and very broad features found by Tytler et al. are artifacts caused by noise and blending, an accurate assessment of their reality will require a careful analysis of simulated spectra like the kind performed here but with S/N appropriate for the Tytler et al. spectra.

5.4 Clustering Properties

The most common way to investigate the clustering properties of quasar absorption line systems along the line of sight is to construct the two-point correlation function (Sargent et al. 1980), which is the distribution of pair-wise line separations in velocity or space. In Figure 8 we show the two-point correlation functions (solid histogram) of the Ly α clouds in Sample 1 against velocity separation: $\Delta v = \frac{(z_2 - z_1)c}{1 + \langle z \rangle}$, where c is the speed of light. The upper panel is for the real data and lower panel for the simulation. The waving continuous curves in each case indicate the $\pm 1\sigma$ standard deviation expected from randomly distributed (ie, unclustered) clouds as determined from Monte Carlo simulations. The lack of any significant clustering signal in the simulation is consistent with the

input cloud distribution, which is random other than a general increase of line density with $N(z) \propto (1+z)^{2.75}$. The simulation results also indicate that at velocity separations $\Delta v < 50 \text{ km s}^{-1}$ or so, any information on clustering is lost owing to the intrinsic width of the lines and possibly blending, too. There is a weak clustering signal at $100 < \Delta v < 160 \text{ km s}^{-1}$ in the observed cloud distribution for $13.0 < \log N < 15.0$. Monte Carlo simulations indicate that the probability of finding 3 consecutive velocity bins with deviations at least as large as those observed at $100 < \Delta v < 160 \text{ km s}^{-1}$ in the real data for randomly distributed clouds is 3.7% (the probability doubles if negative deviations or anti-clustering are also considered). Thus the statistical significance of this clustering signal is only marginal. The significance of this clustering signal drops for any other choices of column density range.

5.5 Proximity Effect

The proximity effect, which is the deficit of Ly α clouds near a quasar emission redshift, can be used to estimate the mean intensity of the UV ionizing background at that redshift assuming the effect is caused by the enhanced UV radiation from the nearby quasar (Bajtlik et al. 1988). This is generally done by comparing the number density of Ly α lines above a certain completeness limit (in equivalent width or column density) near the quasar emission line with that expected from the general distribution of the Ly α clouds determined from regions far away from the Ly α emission. Such an approach, however, is not very practical here because the completeness limit in $N(\text{H I})$ not only depends on the S/N of the data, but also on the degree of blending (or equivalently the mean density of lines); both are very different near the Ly α emission. Figure 6 suggests that if we are to use a constant column density cutoff to ensure completeness of the sample, then the cutoff has to be at least as large as $\log N=13.5$, which would severely limit the number of lines in the sample. For this reason, we adopt the following approach.

We divide the observed spectrum into 100 Å bins starting from the emission redshift z_{em} , and calculate the mean D_A value of each bin, where $D_A = \langle 1 - f_o/f_c \rangle$ with f_o and f_c being the observed flux and the estimated continuum. Thus D_A is a measure of the mean depression of the quasar continuum by the ensemble of Ly α absorption lines and whatever metal lines that are present. These D_A values are plotted as open circles in Figure 9. The fact that the value of $1 - D_A$ in the bin closest to z_{em} is significantly above all others is evidence for the proximity effect. We then perform a number of simulations as

described in section 4 and fold in the proximity effect by modifying the $N(\text{H I})$ of each cloud according to the equation $N(\text{H I})' = N(\text{H I}) / (1 + \omega(z))$, where $\omega(z)$ is the ratio of quasar flux at redshift z to the flux of the UV background (see Lu et al. 1991 for derivations of the relevant equations). Note that absorption lines associated with metal systems are assumed to be unaffected. We then adjust the mean intensity of the UV background at the Lyman limit frequency, J_ν^{LL} , until the D_A distributions from the simulated spectra match that from the observed spectrum. The results are shown in Figure 9, where the dotted lines indicate the D_A values estimated from 25 simulations with $J_\nu^{LL} = 2 \times 10^{-22} \text{ erg s}^{-1} \text{ cm}^{-2} \text{ Hz}^{-1} \text{ sr}^{-1}$. The flux of Q 0000–26 at the Lyman limit frequency is estimated to be $10^{-27} \text{ erg s}^{-1} \text{ cm}^{-1} \text{ Hz}^{-1}$ from the spectrum published by Sargent, Steidel, & Boksenberg (1989). We have adopted an emission redshift of 4.127 for Q 0000–26, which is the redshift of the highest-redshift Ly α line detected in the spectrum other than the associated metal system at $z = 4.133$. This redshift agrees well with the value, $z_{em} = 4.124$, estimated from the low ionization emission lines of O I $\lambda 1302$ /Si II $\lambda 1304$ (Brian Espey, private communication). Studies (cf. Gaskell 1982; Espey et al. 1989) have shown that emission lines of low ionization species provide a better indication of the systemic redshift of quasars than high ionization lines. The adopted z_{em} is approximately 1000 km s^{-1} higher than the published redshift of 4.111 by Sargent et al. (1989), which was estimated from the Ly α /N V emission. We conclude that $J_\nu^{LL} \sim 2 \times 10^{-22} \text{ erg s}^{-1} \text{ cm}^{-2} \text{ Hz}^{-1} \text{ sr}^{-1}$ at $z \sim 4.1$ with an uncertainty of about a factor of 2 based on experimentations with the simulations.

We see no obvious difference in the distribution of b values for clouds near the Ly α emission and for clouds elsewhere.

6 DISCUSSION

6.1 The Importance of Numerical Simulations

Throughout the course of this work, we are struck by the amount of information we have gained from analyses of simulated Ly α forest spectra. Although fitting the simulated spectra considerably increase the workload, the effort is nicely rewarded. The simulations have helped us to understand the biases in the derived N - b relation, to gauge the reality of the very narrow and the very broad lines, to make corrections for the incompleteness in the derived column density distribution, and to derive J_ν from the proximity effect analysis. Without such simulations, it would have been very difficult to interpret some of the results and to derive unbiased Doppler width and column density distributions. While

such simulations may have limited use at much lower redshifts where the line density is relatively low and blending is less severe, they are certainly very valuable at the high redshift studied here.

6.2 Evolution of Cloud Properties

The index, $\beta = -1.46 \pm 0.06$, for the H I column density distribution of the clouds in $12.3 < \log N < 14.5$ found here at $3.4 < z < 4.0$ is identical to the value, $\beta = -1.46 \pm 0.05$ found by Hu et al. (1995) at $2.5 < z < 3.1$ based on a similar analysis. Thus there is no obvious evidence for an intrinsic evolution in the column density distribution of the clouds between these redshifts.

The fact that the power-law distribution of Ly α clouds' column density extends to $N(\text{H I})$ at least as low as $2 \times 10^{12} \text{ cm}^{-2}$ has important implications for the study of the He II $\lambda 304$ absorption for these clouds, which is important for determining the ionization level of the absorbing gas. The He II absorption has been detected toward three directions (Jakobsen et al. 1994; Tytler et al. 1995; Davidsen et al. 1996). Because the expected ratio of $N(\text{He II})/N(\text{H I})$ is in the range of 10-100, the clouds that dominate the He II absorption are those with $N(\text{H I})$ in the range $10^{11} - 10^{13} \text{ cm}^{-2}$, which do not dominate the H I absorption. Thus reliable knowledge of the $N(\text{H I})$ distribution at the low column density end will help to interpret the He II absorption results (cf. Songaila, Hu, & Cowie 1995).

While the $N(\text{H I})$ distribution of the clouds does not show any obvious evolution between $z \sim 2.8$ and $z \sim 3.7$, there are some differences in the Doppler b distributions of the clouds between these two epochs. In particular, both the mean b value ($\langle b \rangle = 23 \text{ km s}^{-1}$) and the cutoff b value ($b_{cut} = 15 \text{ km s}^{-1}$) found in this study at $\langle z \rangle = 3.7$ are smaller than the corresponding values, 28 and 20 km s^{-1} , found by Hu et al. (1995) for $\langle z \rangle = 2.8$. Although our estimate of $\langle b \rangle = 23 \text{ km s}^{-1}$ may be uncertain by 2-3 km s^{-1} , simulation results indicate that $\langle b \rangle$ for our sample of Ly α clouds is very unlikely to be as large as 28 km s^{-1} . In particular, we consider the difference in the values of b_{cut} between the two studies quite robust based on the discussion in §5.1.

That Ly α clouds appear narrower at higher redshifts has been noted before by Williger et al. (1994), who studied the Ly α forest in the $z_{em} = 4.5$ quasar BR 1033–0327. The most straightforward interpretation of the cutoff b value is that it reflects the temperature of the clouds broadened purely by thermal motions. If so, then the corresponding

temperatures for $b_{cut} = 20$ and 15 km s^{-1} are $2.4 \times 10^4 \text{ K}$ and $1.4 \times 10^4 \text{ K}$, respectively. However, this interpretation may only be partially correct. Recent cosmological simulations (Cen et al. 1994; Petitjean et al. 1995; Zhang et al. 1995; Hernquist et al. 1996; Miralda-Escude et al. 1996) all indicate that, at $z \sim 2-4$, Ly α clouds with $N(\text{H I}) < 10^{16} \text{ cm}^{-2}$ appear to be associated with low density regions of the universe in filaments, sheets, and voids. In particular, the relatively high column density Ly α clouds are associated with sheets and filaments with typical overdensity $\rho/\langle\rho\rangle \sim 1-10$ where thermal broadening generally dominates or is comparable to broadening from bulk motion, while the very low column density clouds are associated with density enhancement in voids ($\rho/\langle\rho\rangle < 1$) for which the absorption is usually broadened by bulk motions as the gas expands with the Hubble flow (Miralda-Escude et al. 1996). Hence the cutoff b value at the low column density end may be governed by bulk motions rather than by thermal motions. In addition, the work of Miralda-Escude et al. (1996) indicates an increase in the mean temperature of the absorbing gas (at least for $N(\text{H I}) > 13.5$) with decreasing redshift over the range $2 < z < 4$ (see their figure 9), in qualitative agreement with observations. Quantitative comparisons with published cosmological simulation results are not terribly meaningful as the Doppler width distributions given by the various groups are determined in ways different from Voigt profile fitting.

There may also be some differences in the clustering properties of the clouds between $\langle z \rangle = 2.8$ and $\langle z \rangle = 3.7$. Webb (1987) found marginally significant evidence for clustering of Ly α clouds (ie, those devoid of obvious metal lines) on velocity scales of 50-150 km s^{-1} . Cristiani et al. (1995) and Hu et al. (1995) also found evidence for clustering on similar scales, although Rauch et al. (1992) did not. In particular, Cristiani et al. showed that the higher column density Ly α clouds show stronger clustering than the lower column density Ly α clouds. The presence of weak but significant clustering in the line of sight distributions of Ly α clouds and the recent detections of weak C IV absorption associated with the relatively high column density Ly α clouds (Cowie et al. 1995; Tytler et al. 1995; Sargent et al. 1996) suggest that there may be a continuous distribution in the physical properties of the quasar absorption clouds from the heavy metal systems to the traditional Ly α forest clouds. However, we do not find any strong evidence for clustering in our data for clouds of any column density. A similar study of Ly α clouds in the spectrum of a $z_{em} = 4.5$ quasar by Williger et al. (1994) did not find evidence for clustering either. These results may suggest that the clustering of Ly α clouds at $z \geq 4$ is lower than at lower redshift. This interpretation is consistent with results from

recent hydrodynamic cosmological simulations (Petitjean et al. 1995; Zhang et al. 1995; Hernquist et al. 1996; Miralda-Escude et al. 1996), which suggest that Ly α clouds at $2 < z < 4$ arise from filaments and sheets (and sometimes in voids) of low density material in between collapsed objects. Since smaller structures coalesce and form progressively larger structures in these kind of models, it may be expected that the clustering strength of the Ly α clouds should increase with time (ie, decreasing redshift) as the clouds gradually fall towards collapsed objects (galaxies, cluster of galaxies) which are obviously clustered. The models can also explain why higher column density clouds cluster more strongly. The recent finding that low redshift Ly α clouds ($z \sim 0.5$) show significant clustering around metal systems (Bahcall et al. 1996) also supports this interpretation.

Finally, our estimated value of J_ν at $z \sim 4.1$ is very similar to that at $z = 4.5$ estimated by Williger et al. (1994). Giallongo et al. (1996), using a sample of 10 quasar spectra obtained at a median resolution of 11 km s^{-1} , estimated a value of $J_\nu = (5 \pm 1) \times 10^{-22} \text{ erg s}^{-1} \text{ cm}^{-2} \text{ Hz}^{-1} \text{ sr}^{-1}$ over the redshift range $2.0 < z < 4.1$. Our estimate of J_ν at $z \sim 4.1$ is somewhat lower than the Giallongo et al. estimate, but nonetheless may be consistent with their value since Giallongo et al. did find some evidence for a drop of J_ν toward higher redshift. These values are also consistent with those expected if quasars are the main sources of UV ionizing photons at these redshifts (Haardt & Madau 1996). Thus it appears that quasars can provide all the UV ionizing photons in the intergalactic space at least up to the redshift of 4.5 or so, and there is no need to invoke other significant sources of UV photons. This drop in J_ν toward higher redshift will certainly affect the ionization conditions in Ly α clouds and in metal absorption clouds.

7 SUMMARY

We present a high resolution (FWHM=6.6 km s $^{-1}$), high S/N (~ 30) spectrum of the $z_{em} = 4.127$ quasar Q 0000–26 obtained with the Keck telescope. Voigt profiles were fitted to the Ly α absorption lines in order to derive the H I column density and Doppler width distributions of the clouds. Simulated Ly α forest spectra with matching characteristics were also analyzed in order to understand the effects of line blending/blanketing and noise in the data. The main results, applicable at a mean redshift of $\langle z \rangle = 3.7$, are summarized below.

1. The column density distribution, after corrections for incompleteness resulting from line blanketing, is well described by a power law function with index $\beta = -1.55 \pm 0.05$ over

the column density range of $12.6 < \log N(\text{HI}) < 16.0$. A similar fit over the column density range $12.3 < \log N(\text{HI}) < 14.5$ yields $\beta = 1.46 \pm 0.06$, which hints a possible steepening of the distribution at $\log N > 14.5$.

2. The Doppler width distribution is consistent with a Gaussian function with a mean of 23 km s^{-1} and a dispersion of 8 km s^{-1} , but truncated at 15 km s^{-1} , *ie*, no clouds with $b < 15 \text{ km s}^{-1}$ are required to describe the data.

3. There is no significant evidence for an intrinsic correlation between the Doppler width and H I column density of the clouds. The relative lack of clouds with low- N and high- b in the observed distribution (figures 3 and 4), which creates an apparent correlation between N and b , can be understood in terms of measurement biases (§5.1). On the other hand, if indeed there is an intrinsic lack of Ly α clouds with low- N and high- b , such an effect will be difficult to recognize.

4. While the H I column density distribution found here is consistent with that derived from similar studies at lower redshifts (cf. Hu et al. 1995), both the mean Doppler width (23 km s^{-1}) and the cutoff value (15 km s^{-1}) are lower than the similar values determined by Hu et al. for lower redshift clouds (28 km s^{-1} and 20 km s^{-1} , respectively, at $\langle z \rangle = 2.8$). Thus clouds are on average cooler at the higher redshifts studied here.

5. For clouds with $13.0 < \log N(\text{H I}) < 15.0$, We find a marginally significant ($\sim 2\sigma$) clustering signal in the two-point correlation function in the velocity interval $100 < \Delta v < 160 \text{ km s}^{-1}$.

6. Analyses of the proximity effect indicate a value of $J_\nu \sim 2 \times 10^{-22} \text{ erg s}^{-1} \text{ cm}^{-2} \text{ Hz}^{-1} \text{ sr}^{-1}$ for the mean intensity of the metagalactic UV ionizing background at $z \sim 4.1$, which is consistent with the interpretation that quasars provide the bulk of UV ionizing photons at this high redshift.

We are indebted to Bob Carswell for kindly providing the VPFIT software used for this project. We thank Tom Barlow for help in reducing the data with his own software, Brian Espey for communicating the emission redshift of Q 0000–26, and Michael Rauch for useful discussion and for commenting on an earlier draft of the paper. We also thank the referee, Greg Bothun, for many helpful comments. The W. M. Keck Observatory is operated as a scientific partnership between the California Institute of Technology and the

University of California; it was made possible by the generous financial support of the W. M. Keck Foundation. We thank Steven Vogt and the HIRES team for building the HIRES spectrograph, and the observatory staff for expert assistance with the observations. Support for this work was provided by NASA through grant numbers HF1062.01-94A (LL) and HF1040.01-92A (DSW) from the Space Telescope Science Institute, which is operated by the Association of Universities for Research in Astronomy, Inc., for NASA under contract NAS5-26555. WWS acknowledges support from NSF grant AST92-21365. M. Takada-Hidai appreciates support from the General Research Organization, Tokai University, which made it possible for him to stay at Caltech during September 1995 - March 1996.

REFERENCE

- Bahcall, J.N. et al., 1993, *ApJS*, 87, 1
- Bahcall, J.N. et al., 1996, *ApJ*, 457, 19
- Bajtlik, S., Duncan, R.C., & Ostriker, J.P. 1988, *ApJ*, 327, 570
- Carswell, R.F., in *QSO Absorption Lines: Probing the Universe*, eds. J.C. Blades, D.A. Turnshek, & C.A. Norman (Cambridge University Press), p.91
- Carswell, R.F., Webb, J.K., Baldwin, J.A., & Atwood, B. 1987, *ApJ*, 319, 709
- Cen, R., Maralda-Escude, J., Ostriker, J.P., & Rauch, M. 1994, *ApJ*, 437, L9
- Cowie, L.L., Songaila, A., Kim, T-S, & Hu, E.M. 1995, *AJ*, 109, 1522
- Cristiani, S., D’Odorico, S., Fontana, A., Giallongo, E., & Savaglio, S. 1995, *MNRAS*, 273, 1016
- Davidson, A.F., Kriss, G.A., & Zheng, W. 1996, *Nature*, submitted
- Espey, B.R., Carswell, R.F., Bailey, J.A., Smith, M.G., & Ward, M.J. 1989, *ApJ*, 342, 666
- Gaskell, C.M. 1982, *ApJ*, 263, 79
- Giallongo, E., Cristiani, S., D’Odorico, S., Fontana, A., & Savaglio, S. 1996, preprint
- Haardt, F., & Madau, P. 1996, *ApJ*, in press
- Hernquist, L., Katz, N., Weinberg, D.H., & Miralda-Escude, J. 1996, *ApJ*, in press
- Hu, E.M., Kim, T-S, Cowie, L.L., & Songaila, A. 1995, *AJ*, 110, 1526
- Jakobsen, P., Boksenberg, A., Deharveng, J.M., Greenfield, P., Jedrzejewski, R., & Paresce, F 1994, *Nature*, 370, 35
- Lu, L. 1991, *ApJ*, 379, 99
- Lu, L., Wolfe, A.M., & Turnshek, D.A. 1991, *ApJ*, 367, 19
- Miralda-Escude, J., Cen, R., Ostriker, J.P., & Rauch, M. 1996, *ApJ*, submitted
- Petitjean, P., Mucket, J.P., & Kates, R.E. 1995, *A&A*, 295, L9
- Petitjean, P., Webb, J.K., Rauch, M., Carswell, R.F., & Lanzetta, K. 1993 *MNRAS*, 262, 499
- Rauch, M., Carswell, R.F., Chaffee, F.H., Foltz, C.B., Webb, J.K., Weymann, R.J., Bechtold, J., & Green, R.F. 1992, *ApJ*, 390, 387
- Rauch, M., Carswell, R.F., Webb, J.K., & Weymann, R.J. 1993, *MNRAS*, 260, 589
- Sargent, W.L.W., Boksenberg, A., & Steidel, C.C. 1988, *ApJS*, 68, 639
- Sargent, W.L.W., Steidel, C.C., & Boksenberg, A. 1989, *ApJS*, 69, 703
- Sargent, W.L.W., Young, P.J., Boksenberg, A., & Tytler, D. 1980, *ApJS*, 42, 41
- Sargent, W.L.W., Womble, D.S., Barlow, T.A., & Lyons, R.S. 1996, in preparation

- Songaila, A., Hu, E.M., Cowie, L.L. 1995, *Nature*, 375, 124
- Steidel, C.C. 1990, *ApJ*, 72, 1
- Tripp, T.M., Lu, L., & Savage, B.D. 1996, *ApJS*, 102, 239
- Tytler, D., Fan, X-M, Burles, S., Cottrell, L., Davis, C., Kirkman, D., & Zuo, L. 1995, in *Quasar Absorption Lines*, ed. G. Meylan (Springer-Verlag), p.289
- Vogt, S. 1992, in *High Resolution spectroscopy with the VLT*, ed. M.-H. Ulrich (Garching:ESO), 223
- Webb, J.K. 1987, in *Observational Cosmology*, eds. A. Hewett, G. Burbidge, & L.Z.Fang (Reidel, Dordrecht), p803
- Williger, G.M., Baldwin, J.A., Carswell, R.F., Cooke, A.J., Hazard, C., Irwin, M.J., McMahon, R.G., & Storrie-Lombardi, L.J. 1994, *ApJ*, 428, 574
- Zhang, Y., Anninos, P., & Norman, M.L. 1995, *ApJ*, 453, L57

FIGURE CAPTIONS

Figure 1 Keck HIRES spectrum of Q 0000–26 in arbitrary flux units. Only the Ly α forest portion is shown in order to illustrate the adopted continuum level (smooth solid curve). Note the damped Ly α absorption at $z_{abs} = 3.39$ or $\lambda = 5337 \text{ \AA}$. The spectral region blocked out by the damped Ly α absorption (indicated by the horizontal bar) will be omitted from Figure 2.

Figure 2 Continuum-normalized Keck HIRES spectrum of Q 0000–26. The lower spectrum in each panel is the 1σ error spectrum. Absorption lines at $\lambda > 5380 \text{ \AA}$ are marked and listed in Table 1. The results of VPFIT to the Ly α forest region between $5380\text{--}6250 \text{ \AA}$ are shown as smooth curves superimposed on the spectrum. Note that the damped Ly α absorption at $z_{abs} = 3.39$ has been removed. The spectral region between $5309\text{--}5367 \text{ \AA}$ is not shown because it is at the bottom of the damped Ly α absorption where the observed flux is zero.

Figure 3 Distributions of b vs $\log N$ for clouds in Sample 1 for Q 0000–26 (upper panel) and for the simulation (lower panel). The dashed line represents $b_{cut} = 15 \text{ km s}^{-1}$.

Figure 4 Distributions of b vs $\log N$ for clouds in Sample 2 for Q 0000–26 (upper panel) and for the simulation (lower panel). Formal error bars are from VPFIT. The dashed line represents $b_{cut} = 15 \text{ km s}^{-1}$.

Figure 5 Distribution of b vs $\log N$ for clouds in Sample 2 for a simulation where the input $b_{cut} = 18 \text{ km s}^{-1}$ rather than 15 km s^{-1} . These two cutoff values are indicated by the dotted lines.

Figure 6 Column density distribution of Ly α clouds in Sample 1. The directly measured distributions from profile fitting are shown as histograms in the upper panel for the observation (solid) and the simulation (dotted), with the dashed straight line representing the input distribution to the simulation. The observed distribution, after corrections for incompleteness using the simulation results in the column density range $12.3 < \log N < 13.5$, is shown as histogram in the lower panel, where the dashed line represents the best power-law fit over the column density range $12.6 < \log N < 16.0$ and the dotted line represents a similar fit over $12.3 < \log N < 14.5$.

Figure 7 Distributions of Doppler width for Ly α clouds in Sample 1 and Sample 2 for the observation (solid histograms) and for the simulation (dotted histograms). The dotted smooth curves illustrate the input distribution to the simulation, which is a Gaussian with a mean of 23 km s $^{-1}$ and dispersion of 8 km s $^{-1}$, but truncated at 15 km s $^{-1}$. The input distribution curves have been scaled to roughly match the distributions from profile fitting. The dotted curve/histogram are shifted slightly in the x-direction with respect to the solid histogram for clarity.

Figure 8 Two-point correlation function for Ly α clouds in Sample 1 for the real data (top panel) and for the simulation (lower panel). The waving curves indicate the $\pm\sigma$ standard deviation for randomly distributed clouds.

Figure 9 Proximity effect analysis. The open circles represent D_A measurements in each 100 Å bin from the observed spectrum of Q 0000–26, while the dashed lines represent similar measurements from 25 simulations. The vertical line marks the adopted redshift for Q 0000–26: $z_{em} = 4.127$.

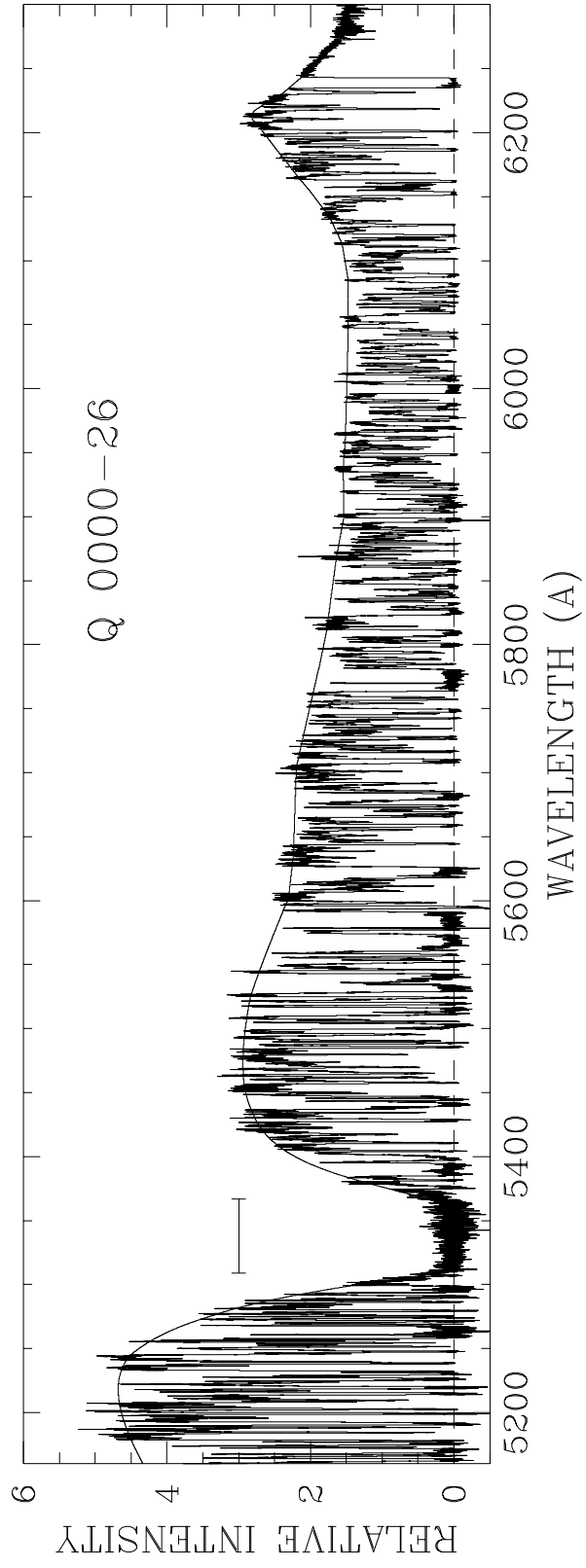


Figure 1

TABLE 1

Q0000–26 ABSORPTION LINE LIST

	λ_{obs}	ID	$z \pm \sigma$	$b \pm \sigma$	$\log N \pm \sigma$	Note
1	5381.53	Ly α	3.426800 \pm 0.000011	23.5 \pm 1.5	14.46 \pm 0.10	
2	5382.97	Ly α	3.427983 \pm 0.000036	32.1 \pm 3.9	13.34 \pm 0.04	
3	5386.66	Ly α	3.431025 \pm 0.000029	64.5 \pm 2.9	15.02 \pm 0.06	
4	5389.06	Ly α	3.432992 \pm 0.000056	25.4 \pm 5.1	13.98 \pm 0.12	
5	5391.68	Ly α (M)	3.435153 \pm 0.000043	62.7 \pm 19.2	15.51 \pm 0.54	1
6	5394.33	Ly α	3.437328 \pm 0.000045	24.3 \pm 1.9	14.38 \pm 0.10	
7	5398.00	Ly α	3.440350 \pm 0.000051	41.5 \pm 4.2	14.63 \pm 0.15	
8	5398.93	Ly α	3.441114 \pm 0.000027	127.5 \pm 2.4	14.61 \pm 0.02	
9	5400.83	Ly α	3.442675 \pm 0.000050	15.9 \pm 5.4	12.89 \pm 0.15	
10	5403.10	Ly α	3.444547 \pm 0.000038	21.6 \pm 4.1	12.88 \pm 0.07	
11	5404.19	Ly α	3.445445 \pm 0.000006	22.2 \pm 0.8	14.16 \pm 0.03	
12	5406.35	Ly α	3.447219 \pm 0.000041	56.8 \pm 4.7	13.26 \pm 0.03	
13	5409.17	Ly α	3.449535 \pm 0.000078	45.7 \pm 8.6	12.99 \pm 0.07	
14	5410.53	Ly α	3.450655 \pm 0.000012	19.3 \pm 1.0	14.15 \pm 0.04	
15	5411.31	Ly α	3.451296 \pm 0.000041	22.1 \pm 3.1	13.40 \pm 0.07	
16	5412.57	Ly α	3.452336 \pm 0.000022	32.7 \pm 2.4	13.30 \pm 0.03	
17	5414.19	Ly α	3.453668 \pm 0.000016	22.9 \pm 1.6	13.14 \pm 0.03	
18	5416.05	Ly α	3.455198 \pm 0.000145	54.5 \pm 13.2	13.18 \pm 0.11	
19	5417.47	Ly α	3.456367 \pm 0.000022	35.2 \pm 1.5	13.71 \pm 0.03	
20	5422.62	Ly α	3.460606 \pm 0.000030	36.6 \pm 2.8	13.27 \pm 0.03	
21	5425.49	Ly α	3.462960 \pm 0.000063	39.2 \pm 5.8	12.93 \pm 0.05	
22	5428.37	Ly α	3.465332 \pm 0.000007	38.6 \pm 1.0	14.74 \pm 0.05	
23	5431.72	Ly α	3.468087 \pm 0.000043	49.1 \pm 3.8	13.27 \pm 0.03	
24	5434.14	Ly α	3.470080 \pm 0.000008	20.7 \pm 0.7	13.69 \pm 0.02	
25	5435.55	Ly α	3.471235 \pm 0.000035	21.9 \pm 3.5	12.78 \pm 0.06	
26	5437.38	Ly α	3.472742 \pm 0.000049	30.8 \pm 3.4	13.64 \pm 0.07	
27	5438.38	Ly α	3.473569 \pm 0.000033	27.5 \pm 3.1	13.77 \pm 0.05	
28	5440.57	Ly α	3.475369 \pm 0.000013	27.3 \pm 1.5	17.84 \pm 0.33	
29	5442.59	Ly α	3.477026 \pm 0.000025	26.7 \pm 2.2	13.81 \pm 0.05	
30	5444.45	Ly α	3.478556 \pm 0.000006	27.0 \pm 1.1	14.74 \pm 0.08	
31	5446.52	Ly α	3.480260 \pm 0.000008	33.0 \pm 0.9	14.15 \pm 0.02	
32	5447.97	Ly α	3.481452 \pm 0.000032	17.1 \pm 3.5	12.67 \pm 0.08	
33	5449.29	Ly α	3.482541 \pm 0.000020	29.3 \pm 2.0	13.44 \pm 0.03	
34	5450.36	Ly α	3.483417 \pm 0.000026	23.0 \pm 2.3	13.16 \pm 0.04	
35	5452.53	Ly α	3.485207 \pm 0.000045	26.2 \pm 4.4	12.73 \pm 0.06	
36	5455.94	Ly α	3.488009 \pm 0.000042	25.4 \pm 4.1	12.84 \pm 0.06	
37	5457.78	Ly α	3.489524 \pm 0.000011	33.1 \pm 1.2	14.28 \pm 0.03	
38	5459.23	Ly α	3.490719 \pm 0.000050	31.5 \pm 4.9	13.17 \pm 0.06	
39	5460.97	Ly α	3.492146 \pm 0.000084	27.4 \pm 6.4	13.09 \pm 0.11	
40	5461.86	Ly α	3.492879 \pm 0.000017	23.6 \pm 1.2	13.79 \pm 0.03	
41	5465.00	Ly α	3.495465 \pm 0.000013	32.5 \pm 0.9	13.98 \pm 0.02	
42	5466.32	Ly α	3.496550 \pm 0.000060	52.2 \pm 3.8	13.63 \pm 0.04	
43	5469.85	Ly α	3.499456 \pm 0.000009	31.0 \pm 0.9	13.81 \pm 0.02	
44	5471.67	Ly α	3.500947 \pm 0.000068	80.3 \pm 9.4	13.56 \pm 0.04	
45	5473.74	Ly α	3.502656 \pm 0.000016	24.1 \pm 1.7	13.16 \pm 0.04	
46	5475.19	Ly α	3.503844 \pm 0.000060	30.7 \pm 6.7	12.65 \pm 0.09	
47	5477.09	Ly α	3.505406 \pm 0.000117	59.0 \pm 13.3	12.80 \pm 0.08	
48	5479.82	Ly α	3.507655 \pm 0.000006	20.8 \pm 0.5	13.59 \pm 0.01	

TABLE 1 — *Continued*

	λ_{obs}	ID	$z \pm \sigma$	$b \pm \sigma$	$\log N \pm \sigma$	Note
49	5481.06	Ly α	3.508678 \pm 0.000024	25.2 \pm 2.5	12.89 \pm 0.04	
50	5482.64	Ly α	3.509974 \pm 0.000019	22.7 \pm 1.9	12.95 \pm 0.04	
51	5485.42	Ly α	3.512262 \pm 0.000005	29.2 \pm 0.8	14.46 \pm 0.03	
52	5486.37	Ly α	3.513040 \pm 0.000480	132.3 \pm 38.2	13.43 \pm 0.06	
53	5488.09	Ly α	3.514456 \pm 0.000107	17.0 \pm 4.8	13.14 \pm 0.31	
54	5488.75	Ly α	3.514996 \pm 0.000024	22.0 \pm 1.3	14.31 \pm 0.05	
55	5490.39	Ly α	3.516351 \pm 0.000007	21.6 \pm 1.3	13.84 \pm 0.05	
56	5490.96	Ly α	3.516818 \pm 0.000259	44.3 \pm 10.3	13.29 \pm 0.22	
57	5494.69	Ly α	3.519887 \pm 0.000092	35.7 \pm 4.4	13.36 \pm 0.10	
58	5495.57	Ly α	3.520613 \pm 0.000023	29.1 \pm 1.1	13.79 \pm 0.04	
59	5497.54	Ly α	3.522228 \pm 0.000013	20.0 \pm 1.3	12.93 \pm 0.02	
60	5498.76	Ly α	3.523235 \pm 0.000067	19.6 \pm 6.8	12.23 \pm 0.12	
61	5499.85	Ly α	3.524134 \pm 0.000018	17.6 \pm 0.9	13.86 \pm 0.04	
62	5500.46	Ly α	3.524634 \pm 0.000018	16.1 \pm 2.0	13.71 \pm 0.05	
63	5502.40	Ly α	3.526225 \pm 0.000011	40.4 \pm 2.3	15.63 \pm 0.16	
64	5504.38	S II 1253	3.390123 \pm 0.000007	9.2 \pm 0.8	14.70 \pm 0.03	2
65	5505.67	Ly α	3.528914 \pm 0.000006	21.7 \pm 0.7	14.22 \pm 0.04	
66	5506.97	Ly α	3.529985 \pm 0.000013	22.7 \pm 1.1	13.39 \pm 0.02	
67	5511.42	Ly α	3.533650 \pm 0.000013	54.2 \pm 1.1	14.40 \pm 0.01	
68	5514.74	Ly α (M)	3.536379 \pm 0.000009	50.4 \pm 1.4	15.44 \pm 0.07	1
69	5519.45	Ly α	3.540255 \pm 0.000006	40.8 \pm 0.9	14.77 \pm 0.04	
70	5522.47	Ly α	3.542734 \pm 0.000042	30.2 \pm 2.8	13.48 \pm 0.04	
71	5523.31	Ly α	3.543429 \pm 0.000037	17.8 \pm 3.3	13.48 \pm 0.11	
72	5524.22	Ly α	3.544181 \pm 0.000021	26.6 \pm 1.3	14.33 \pm 0.05	
73	5528.27	Ly α	3.547506 \pm 0.000170	41.7 \pm 7.0	13.51 \pm 0.15	
74	5531.33	Ly α	3.550023 \pm 0.000052	58.2 \pm 6.6	16.42 \pm 0.52	
75	5532.63	SiII 1260	3.389505 \pm 0.000004	5.6 \pm 0.3	13.50 \pm 0.02	3
76	5532.84	SiII 1260	3.389669 \pm 0.000005	3.4 \pm 0.5	13.21 \pm 0.03	3
77	5533.34	SiII 1260	3.390073 \pm 0.000002	6.4 \pm 0.1	16.33 \pm 0.07	3
78	5533.92	SiII 1260	3.390526 \pm 0.000007	9.9 \pm 0.9	13.12 \pm 0.05	3
79	5534.45	SiII 1260	3.390953 \pm 0.000009	10.0 \pm 1.3	12.66 \pm 0.05	3
80	5534.77	SiII 1260	3.391200 \pm 0.000004	3.8 \pm 0.5	12.83 \pm 0.04	3
81	5535.25	Ly α	3.553252 \pm 0.000022	27.6 \pm 2.7	13.54 \pm 0.04	
82	5537.25	Ly α	3.554892 \pm 0.000048	59.4 \pm 4.7	14.15 \pm 0.03	
83	5538.79	Ly α	3.556162 \pm 0.000024	29.7 \pm 3.0	14.02 \pm 0.05	
84	5541.12	Ly α	3.558082 \pm 0.000017	46.0 \pm 1.6	15.53 \pm 0.09	
85	5546.03	Ly α	3.562119 \pm 0.000010	23.6 \pm 1.0	14.05 \pm 0.03	
86	5547.00	Ly α	3.562917 \pm 0.000031	17.0 \pm 3.5	13.02 \pm 0.10	
87	5548.07	Ly α	3.563798 \pm 0.000042	42.1 \pm 3.9	13.44 \pm 0.04	
88	5551.86	Ly α	3.566910 \pm 0.000175	85.2 \pm 6.0	14.07 \pm 0.09	
89	5552.30	Ly α	3.567277 \pm 0.000016	27.0 \pm 2.8	14.74 \pm 0.15	
90	5554.29	Ly α	3.568913 \pm 0.000075	29.1 \pm 6.4	13.83 \pm 0.14	
91	5554.84	Ly α	3.569362 \pm 0.000034	15.2 \pm 3.7	13.37 \pm 0.28	
92	5557.20	Ly α	3.571310 \pm 0.000025	50.9 \pm 2.0	14.20 \pm 0.04	
93	5557.50	Ly α	3.571554 \pm 0.000017	22.4 \pm 2.1	14.83 \pm 0.19	
94	5559.88	Ly α	3.573509 \pm 0.000043	30.7 \pm 3.1	13.41 \pm 0.08	
95	5561.12	Ly α	3.574528 \pm 0.000020	21.8 \pm 2.7	14.24 \pm 0.09	
96	5562.33	Ly α	3.575524 \pm 0.000108	56.0 \pm 31.0	14.17 \pm 0.24	
97	5563.59	Ly α	3.576562 \pm 0.000059	29.5 \pm 7.5	13.98 \pm 0.25	
98	5566.74	Ly α	3.579157 \pm 0.005447	67.6 \pm 73.5	15.73 \pm 6.09	

TABLE 1 — *Continued*

	λ_{obs}	ID	$z \pm \sigma$	$b \pm \sigma$	$\log N \pm \sigma$	Note
99	5569.92	Ly α	3.581768 \pm 0.000780	35.3 \pm 10.6	18.01 \pm 2.12	
100	5572.78	Ly α	3.584125 \pm 0.000038	32.7 \pm 5.8	14.31 \pm 0.09	
101	5573.85	Ly α	3.585005 \pm 0.000087	24.5 \pm 4.6	13.45 \pm 0.19	
102	5575.55	Ly α	3.586402 \pm 0.000190	67.6 \pm 28.2	13.31 \pm 0.40	
103	5577.48	Ly α	3.587992 \pm 0.000007	24.2 \pm 0.9	14.27 \pm 0.04	
104	5580.61	Ly α (M)	3.590560 \pm 0.000047	25.1 \pm 1.0	18.39 \pm 0.05	1
105	5585.35	Ly α (M)	3.594460 \pm 0.000062	72.6 \pm 12.6	16.65 \pm 0.67	1
106	5589.99	Ly α	3.598279 \pm 0.000032	45.0 \pm 2.0	14.72 \pm 0.05	
107	5593.15	Ly α	3.600878 \pm 0.000067	20.7 \pm 4.7	13.07 \pm 0.11	
108	5594.74	Ly α	3.602187 \pm 0.000013	32.9 \pm 1.4	15.25 \pm 0.11	
109	5598.37	Ly α	3.605172 \pm 0.000017	32.1 \pm 1.2	13.97 \pm 0.02	
110	5599.35	Ly α	3.605978 \pm 0.000083	24.9 \pm 6.2	12.87 \pm 0.16	
111	5606.14	Ly α	3.611564 \pm 0.000054	20.2 \pm 5.5	12.57 \pm 0.10	
112	5607.31	Ly α	3.612524 \pm 0.000026	24.9 \pm 2.3	13.54 \pm 0.04	
113	5608.09	Ly α	3.613166 \pm 0.000031	18.4 \pm 2.6	13.21 \pm 0.09	
114	5609.21	Ly α	3.614085 \pm 0.000032	18.7 \pm 6.1	12.82 \pm 0.24	
115	5610.69	Ly α	3.615306 \pm 0.000153	80.7 \pm 11.9	13.77 \pm 0.03	
116	5611.31	Ly α	3.615815 \pm 0.000015	24.4 \pm 1.8	13.67 \pm 0.05	
117	5613.62	Ly α	3.617716 \pm 0.000014	27.1 \pm 1.4	13.43 \pm 0.02	
118	5615.98	Ly α	3.619660 \pm 0.000024	65.3 \pm 2.8	13.83 \pm 0.01	
119	5618.35	Ly α	3.621608 \pm 0.000014	32.3 \pm 1.5	14.38 \pm 0.03	
120	5619.97	Ly α	3.622944 \pm 0.000072	32.3 \pm 5.6	13.98 \pm 0.10	
121	5623.34	Ly α (M)	3.625714 \pm 0.000053	71.7 \pm 2.0	16.21 \pm 0.10	1
122	5630.38	Ly α	3.631505 \pm 0.000050	50.6 \pm 4.8	13.15 \pm 0.04	
123	5633.62	Ly α	3.634170 \pm 0.000028	37.0 \pm 2.5	13.24 \pm 0.03	
124	5638.52	SiIII 1206	3.673455 \pm 0.000009	15.4 \pm 1.0	12.50 \pm 0.03	
125	5639.51	Ly α	3.639014 \pm 0.000297	92.0 \pm 19.8	12.97 \pm 0.09	
126	5641.14	Ly α	3.640351 \pm 0.000023	25.1 \pm 3.2	12.91 \pm 0.08	
127	5644.41	Ly α	3.643045 \pm 0.000054	22.6 \pm 2.1	14.40 \pm 0.27	
128	5644.85	Ly α	3.643407 \pm 0.001519	29.6 \pm 45.3	13.36 \pm 2.55	
129	5646.75	Ly α	3.644972 \pm 0.000106	101.6 \pm 8.8	13.70 \pm 0.03	
130	5647.11	Ly α	3.645267 \pm 0.000022	22.4 \pm 2.5	13.04 \pm 0.07	
131	5650.71	Ly α	3.648225 \pm 0.000013	37.8 \pm 1.2	13.48 \pm 0.01	
132	5653.07	Ly α	3.650166 \pm 0.000033	46.3 \pm 3.5	13.12 \pm 0.03	
133	5655.42	Ly α	3.652099 \pm 0.000008	37.5 \pm 0.8	13.80 \pm 0.01	
134	5658.34	Ly α	3.654507 \pm 0.000064	54.5 \pm 5.2	13.99 \pm 0.20	
135	5658.56	Ly α	3.654684 \pm 0.000010	29.6 \pm 1.9	15.19 \pm 0.12	
136	5661.35	Ly α	3.656976 \pm 0.000013	40.6 \pm 1.5	13.50 \pm 0.01	
137	5663.60	Ly α	3.658830 \pm 0.000029	46.2 \pm 3.2	13.16 \pm 0.02	
138	5665.71	Ly α	3.660566 \pm 0.000005	24.0 \pm 0.5	14.05 \pm 0.01	
139	5667.06	Ly α	3.661678 \pm 0.000007	19.9 \pm 0.7	14.03 \pm 0.02	
140	5668.59	Ly α	3.662935 \pm 0.000006	27.1 \pm 1.3	14.97 \pm 0.09	
141	5670.38	Ly α	3.664406 \pm 0.000013	36.8 \pm 2.2	13.78 \pm 0.02	
142	5671.70	Ly α	3.665496 \pm 0.000008	24.8 \pm 0.6	13.94 \pm 0.01	
143	5674.04	Ly α	3.667418 \pm 0.000004	19.6 \pm 0.7	14.60 \pm 0.06	
144	5674.52	Ly α	3.667816 \pm 0.000058	74.0 \pm 5.0	13.55 \pm 0.03	
145	5676.66	Ly α	3.669574 \pm 0.000026	18.6 \pm 2.2	13.04 \pm 0.06	
146	5677.70	Ly α	3.670428 \pm 0.000028	29.2 \pm 3.7	13.51 \pm 0.05	
147	5678.91	Ly α	3.671426 \pm 0.000013	24.0 \pm 1.7	14.09 \pm 0.03	
148	5681.72	Ly α (M)	3.673733 \pm 0.000013	53.1 \pm 2.2	15.86 \pm 0.13	1

TABLE 1 — *Continued*

	λ_{obs}	ID	$z \pm \sigma$	$b \pm \sigma$	$\log N \pm \sigma$	Note
149	5685.32	Ly α	3.676695 \pm 0.000009	17.3 \pm 1.1	13.89 \pm 0.04	
150	5685.72	Ly α	3.677029 \pm 0.000035	54.5 \pm 2.3	13.76 \pm 0.03	
151	5688.33	Ly α	3.679171 \pm 0.000029	34.5 \pm 2.8	13.18 \pm 0.03	
152	5690.93	Ly α	3.681311 \pm 0.000042	61.4 \pm 2.2	13.81 \pm 0.02	
153	5691.72	Ly α	3.681964 \pm 0.000013	21.4 \pm 1.4	13.60 \pm 0.04	
154	5694.91	Ly α	3.684582 \pm 0.000039	61.8 \pm 3.7	13.37 \pm 0.02	
155	5698.05	Ly α	3.687168 \pm 0.000033	36.0 \pm 2.9	13.15 \pm 0.03	
156	5700.99	Ly α	3.689590 \pm 0.000013	34.8 \pm 1.1	13.60 \pm 0.01	
157	5705.43	FeII 2344	1.433836 \pm 0.000002	1.3 \pm 0.4	12.62 \pm 0.12	4
158	5706.26	FeII 2344	1.434187 \pm 0.000002	6.8 \pm 0.4	12.73 \pm 0.02	4
159	5707.88	Ly α	3.695254 \pm 0.000016	31.9 \pm 1.0	14.30 \pm 0.03	
160	5709.68	Ly α	3.696737 \pm 0.000019	41.9 \pm 1.3	14.44 \pm 0.02	
161	5712.64	Ly α	3.699170 \pm 0.000060	52.8 \pm 6.9	13.14 \pm 0.04	
162	5714.15	Ly α	3.700413 \pm 0.000064	19.0 \pm 6.5	12.39 \pm 0.16	
163	5715.88	O I 1302	3.389505 \pm 0.000000	5.6 \pm 0.0	15.25 \pm 0.13	5
164	5716.62	O I 1302	3.390073 \pm 0.000000	6.4 \pm 0.0	17.91 \pm 0.07	5
165	5717.21	O I 1302	3.390526 \pm 0.000000	9.9 \pm 0.0	14.04 \pm 0.05	5
166	5717.76	O I 1302	3.390953 \pm 0.000000	10.0 \pm 0.0	13.81 \pm 0.04	5
167	5718.08	O I 1302	3.391200 \pm 0.000000	3.8 \pm 0.0	13.18 \pm 0.12	5
168	5719.19	Ly α	3.704561 \pm 0.000012	36.4 \pm 1.1	13.74 \pm 0.01	
169	5721.27	Ly α	3.706270 \pm 0.000009	23.2 \pm 0.8	13.52 \pm 0.01	
170	5723.59	Ly α	3.708174 \pm 0.000046	53.5 \pm 4.3	13.22 \pm 0.03	
171	5725.54	SiII 1304	3.389505 \pm 0.000004	5.6 \pm 0.3	13.50 \pm 0.02	3
172	5725.75	SiII 1304	3.389669 \pm 0.000005	3.4 \pm 0.5	13.21 \pm 0.03	3
173	5726.28	SiII 1304	3.390073 \pm 0.000002	6.4 \pm 0.1	16.33 \pm 0.07	3
174	5726.87	SiII 1304	3.390526 \pm 0.000007	9.9 \pm 0.9	13.12 \pm 0.05	3
175	5727.40	Ly α	3.711310 \pm 0.000038	49.0 \pm 2.0	13.91 \pm 0.02	
176	5727.43	SiII 1304	3.390953 \pm 0.000009	10.0 \pm 1.3	12.66 \pm 0.05	3
177	5727.75	SiII 1304	3.391200 \pm 0.000004	3.8 \pm 0.5	12.83 \pm 0.04	3
178	5727.96	Ly α	3.711770 \pm 0.000012	16.4 \pm 1.0	13.96 \pm 0.05	
179	5730.22	Ly α	3.713633 \pm 0.000016	28.1 \pm 1.5	13.30 \pm 0.02	
180	5731.42	Ly α	3.714616 \pm 0.000018	22.5 \pm 2.1	13.25 \pm 0.06	
181	5732.63	Ly α	3.715616 \pm 0.000047	50.5 \pm 6.3	13.52 \pm 0.05	
182	5734.24	Ly α	3.716941 \pm 0.000005	21.6 \pm 0.5	13.96 \pm 0.01	
183	5735.71	Ly α	3.718148 \pm 0.000086	22.6 \pm 8.8	12.93 \pm 0.44	
184	5736.62	Ly α	3.718897 \pm 0.000113	49.0 \pm 4.7	13.72 \pm 0.10	
185	5736.69	Ly α	3.718953 \pm 0.000022	13.0 \pm 2.7	13.00 \pm 0.14	
186	5739.41	Ly α	3.721193 \pm 0.000055	36.1 \pm 3.5	13.38 \pm 0.05	
187	5740.13	Ly α	3.721783 \pm 0.000024	16.0 \pm 3.0	12.84 \pm 0.15	
188	5741.24	Ly α	3.722699 \pm 0.000008	18.2 \pm 0.8	13.31 \pm 0.01	
189	5742.47	Ly α	3.723704 \pm 0.000005	23.0 \pm 0.6	14.24 \pm 0.02	
190	5744.06	Ly α	3.725019 \pm 0.000059	44.4 \pm 7.1	12.95 \pm 0.05	
191	5746.00	Ly α	3.726613 \pm 0.000008	26.0 \pm 0.7	13.88 \pm 0.01	
192	5748.33	Ly α (M)	3.728526 \pm 0.000012	44.8 \pm 1.8	15.04 \pm 0.06	1
193	5750.20	Ly α	3.730067 \pm 0.000174	42.4 \pm 8.7	13.17 \pm 0.16	
194	5753.95	Ly α	3.733154 \pm 0.000089	103.6 \pm 11.3	13.27 \pm 0.03	
195	5754.27	Ly α	3.733418 \pm 0.000007	22.7 \pm 0.7	13.57 \pm 0.01	
196	5757.29	Ly α	3.735898 \pm 0.000007	29.8 \pm 0.6	14.27 \pm 0.02	
197	5758.79	Ly α	3.737136 \pm 0.000007	26.4 \pm 0.8	13.89 \pm 0.01	
198	5760.17	Ly α	3.738264 \pm 0.000036	33.7 \pm 3.1	13.09 \pm 0.03	

TABLE 1 — *Continued*

	λ_{obs}	ID	$z \pm \sigma$	$b \pm \sigma$	$\log N \pm \sigma$	Note
199	5762.57	Ly α	3.740245 \pm 0.000048	26.5 \pm 4.3	12.66 \pm 0.06	
200	5764.86	Ly α	3.742126 \pm 0.000010	43.0 \pm 1.2	14.95 \pm 0.04	
201	5767.93	Ly α	3.744653 \pm 0.000009	38.8 \pm 1.4	15.97 \pm 0.13	
202	5771.61	Ly α (M)	3.747682 \pm 0.000105	27.9 \pm 1.2	16.67 \pm 0.66	1
203	5776.74	Ly α (M)	3.751896 \pm 0.000124	110.2 \pm 3.5	15.99 \pm 0.09	1
204	5782.96	Ly α	3.757014 \pm 0.000014	38.5 \pm 1.4	13.66 \pm 0.01	
205	5784.79	Ly α	3.758518 \pm 0.000015	22.4 \pm 1.0	14.17 \pm 0.03	
206	5785.73	Ly α	3.759291 \pm 0.000033	22.7 \pm 3.1	13.47 \pm 0.06	
207	5786.95	Ly α	3.760296 \pm 0.000029	31.2 \pm 4.2	13.27 \pm 0.05	
208	5788.66	Ly α	3.761702 \pm 0.000014	34.1 \pm 1.5	14.00 \pm 0.01	
209	5789.86	Ly α	3.762692 \pm 0.000032	22.9 \pm 2.8	13.27 \pm 0.07	
210	5791.92	Ly α	3.764383 \pm 0.000141	87.8 \pm 23.2	13.45 \pm 0.10	
211	5793.50	Ly α	3.765682 \pm 0.000060	21.7 \pm 3.9	13.62 \pm 0.28	
212	5794.18	Ly α	3.766244 \pm 0.000155	35.1 \pm 8.7	13.86 \pm 0.17	
213	5795.72	Ly α	3.767508 \pm 0.000107	38.4 \pm 7.4	13.15 \pm 0.10	
214	5799.59	Ly α	3.770697 \pm 0.000009	44.3 \pm 1.5	15.20 \pm 0.08	
215	5801.88	Ly α	3.772579 \pm 0.000191	213.0 \pm 13.9	14.05 \pm 0.03	
216	5803.07	Ly α	3.773560 \pm 0.000011	20.6 \pm 1.0	13.58 \pm 0.02	
217	5805.05	Ly α	3.775189 \pm 0.000016	17.8 \pm 1.8	13.12 \pm 0.05	
218	5806.48	Ly α	3.776359 \pm 0.000010	20.7 \pm 0.9	13.83 \pm 0.02	
219	5809.31	Ly α	3.778688 \pm 0.000009	42.2 \pm 1.4	16.94 \pm 0.18	
220	5813.33	Ly α	3.781999 \pm 0.000038	10.1 \pm 3.8	12.29 \pm 0.12	
221	5814.21	SiIII 1206	3.819071 \pm 0.000008	11.3 \pm 0.7	12.63 \pm 0.02	
222	5816.36	Ly α	3.784487 \pm 0.000028	16.2 \pm 2.5	12.73 \pm 0.05	
223	5817.53	Ly α	3.785449 \pm 0.000030	16.8 \pm 2.7	12.73 \pm 0.06	
224	5819.44	Ly α	3.787019 \pm 0.000132	50.2 \pm 14.1	12.73 \pm 0.12	
225	5824.53	Ly α	3.791213 \pm 0.000450	56.8 \pm 9.9	14.73 \pm 0.40	
226	5825.67	Ly α	3.792146 \pm 0.000106	22.9 \pm 2.6	17.99 \pm 0.11	
227	5828.11	Ly α	3.794152 \pm 0.000011	21.1 \pm 2.0	14.12 \pm 0.04	
228	5828.93	Ly α	3.794827 \pm 0.000167	56.4 \pm 12.5	13.78 \pm 0.12	
229	5831.53	Ly α (M)	3.796968 \pm 0.000041	52.7 \pm 2.4	14.62 \pm 0.05	1
230	5832.62	Ly α (M)	3.797861 \pm 0.000106	15.6 \pm 3.4	14.25 \pm 0.32	1
231	5834.41	Ly α	3.799335 \pm 0.000007	15.4 \pm 0.8	13.51 \pm 0.03	
232	5834.48	Ly α	3.799392 \pm 0.000112	51.3 \pm 12.2	13.08 \pm 0.09	
233	5836.93	Ly α	3.801406 \pm 0.000005	28.3 \pm 0.6	14.23 \pm 0.02	
234	5838.69	Ly α	3.802859 \pm 0.000008	24.0 \pm 0.7	14.02 \pm 0.01	
235	5839.98	Ly α	3.803916 \pm 0.000009	23.3 \pm 1.0	14.09 \pm 0.02	
236	5841.57	Ly α	3.805229 \pm 0.000012	42.8 \pm 1.6	14.17 \pm 0.01	
237	5843.01	Ly α	3.806414 \pm 0.000021	18.6 \pm 2.7	13.14 \pm 0.07	
238	5844.62	Ly α	3.807736 \pm 0.000009	27.6 \pm 1.6	15.33 \pm 0.14	
239	5846.48	Ly α	3.809262 \pm 0.000014	33.5 \pm 0.9	14.24 \pm 0.01	
240	5848.94	Ly α	3.811293 \pm 0.000038	50.8 \pm 4.0	13.17 \pm 0.03	
241	5850.91	Ly α	3.812910 \pm 0.000007	19.8 \pm 0.6	13.61 \pm 0.01	
242	5851.86	Ly α	3.813692 \pm 0.000027	18.0 \pm 2.9	12.95 \pm 0.08	
243	5852.90	Ly α	3.814545 \pm 0.000014	28.9 \pm 1.9	13.76 \pm 0.02	
244	5854.41	Ly α	3.815792 \pm 0.000010	32.3 \pm 1.4	14.33 \pm 0.02	
245	5857.52	Ly α (M)	3.818349 \pm 0.000031	75.7 \pm 3.3	14.59 \pm 0.04	1
246	5858.11	Ly α (M)	3.818829 \pm 0.000048	20.8 \pm 1.0	18.02 \pm 0.05	1
247	5860.19	C II 1334	3.391195 \pm 0.000004	5.2 \pm 0.4	13.53 \pm 0.03	6
248	5862.66	Ly α	3.822575 \pm 0.000006	22.8 \pm 0.6	14.26 \pm 0.03	

TABLE 1 — *Continued*

	λ_{obs}	ID	$z \pm \sigma$	$b \pm \sigma$	$\log N \pm \sigma$	Note
249	5864.68	Ly α	3.824236 \pm 0.000007	33.3 \pm 1.0	14.69 \pm 0.05	
250	5866.38	Ly α	3.825633 \pm 0.000022	8.0 \pm 2.3	12.41 \pm 0.09	
251	5867.54	Ly α	3.826588 \pm 0.000008	1.4 \pm 2.2	13.05 \pm 1.66	
252	5867.85	Ly α	3.826847 \pm 0.000061	10.7 \pm 5.8	12.47 \pm 0.18	
253	5869.43	Ly α	3.828144 \pm 0.000016	5.7 \pm 1.7	12.55 \pm 0.08	
254	5870.41	Ly α	3.828951 \pm 0.000017	27.5 \pm 1.5	13.48 \pm 0.02	
255	5873.22	Ly α	3.831260 \pm 0.000008	21.9 \pm 0.7	13.94 \pm 0.02	
256	5874.65	Ly α	3.832440 \pm 0.000164	30.7 \pm 11.5	13.04 \pm 0.22	
257	5875.68	Ly α	3.833284 \pm 0.000059	30.3 \pm 3.6	13.51 \pm 0.07	
258	5876.99	Ly α	3.834361 \pm 0.000038	14.2 \pm 4.0	12.51 \pm 0.12	
259	5878.70	Ly α	3.835766 \pm 0.000005	22.1 \pm 0.8	14.46 \pm 0.06	
260	5881.00	Ly α	3.837663 \pm 0.000009	18.0 \pm 0.9	13.45 \pm 0.02	
261	5881.89	Ly α	3.838392 \pm 0.000029	7.9 \pm 3.2	12.30 \pm 0.13	
262	5882.57	Ly α	3.838950 \pm 0.000011	2.7 \pm 1.5	12.44 \pm 0.08	
263	5883.23	Ly α	3.839494 \pm 0.000016	18.4 \pm 1.6	13.17 \pm 0.04	
264	5885.50	Ly α	3.841365 \pm 0.000015	28.7 \pm 1.4	13.67 \pm 0.02	
265	5885.67	Ly α	3.841506 \pm 0.000401	401.8 \pm 39.5	14.11 \pm 0.03	
266	5886.69	Ly α	3.842340 \pm 0.000034	18.3 \pm 3.2	12.89 \pm 0.07	
267	5888.07	Ly α	3.843476 \pm 0.000023	20.7 \pm 1.8	13.46 \pm 0.04	
268	5889.02	Ly α	3.844257 \pm 0.000013	19.6 \pm 1.0	13.93 \pm 0.03	
269	5891.37	Ly α	3.846190 \pm 0.000025	31.1 \pm 2.5	13.32 \pm 0.04	
270	5892.79	Ly α	3.847360 \pm 0.000040	21.1 \pm 4.1	12.78 \pm 0.09	
271	5894.83	Ly α	3.849042 \pm 0.000046	27.5 \pm 4.7	13.00 \pm 0.08	
272	5897.17	Ly α	3.850964 \pm 0.000007	38.1 \pm 1.2	15.68 \pm 0.11	
273	5903.27	Ly α	3.855978 \pm 0.000045	20.4 \pm 2.8	13.79 \pm 0.10	
274	5903.99	Ly α	3.856570 \pm 0.000022	56.2 \pm 1.2	14.27 \pm 0.02	
275	5906.47	Ly α	3.858610 \pm 0.000038	19.2 \pm 1.8	13.76 \pm 0.08	
276	5908.11	Ly α	3.859965 \pm 0.000031	35.6 \pm 3.4	15.33 \pm 0.20	
277	5910.75	Ly α	3.862134 \pm 0.000012	35.1 \pm 2.2	14.49 \pm 0.05	
278	5912.65	Ly α	3.863692 \pm 0.000012	28.8 \pm 1.1	14.13 \pm 0.02	
279	5914.97	Ly α	3.865601 \pm 0.000020	37.8 \pm 1.6	14.45 \pm 0.03	
280	5916.76	Ly α	3.867075 \pm 0.000017	31.0 \pm 1.2	14.28 \pm 0.03	
281	5918.48	Ly α	3.868490 \pm 0.000147	51.9 \pm 23.0	12.66 \pm 0.17	
282	5920.36	Ly α	3.870038 \pm 0.001086	64.6 \pm 66.2	12.88 \pm 0.61	
283	5921.66	Ly α	3.871110 \pm 0.000006	25.8 \pm 1.2	15.23 \pm 0.11	
284	5923.16	Ly α	3.872344 \pm 0.000009	17.7 \pm 0.7	13.63 \pm 0.01	
285	5924.79	Ly α	3.873684 \pm 0.000013	29.5 \pm 0.9	14.23 \pm 0.02	
286	5925.93	Ly α	3.874619 \pm 0.000011	19.4 \pm 1.0	13.90 \pm 0.02	
287	5926.99	Ly α	3.875492 \pm 0.000020	23.4 \pm 2.7	13.21 \pm 0.04	
288	5928.09	Ly α	3.876397 \pm 0.000006	21.7 \pm 0.7	13.72 \pm 0.01	
289	5929.22	Ly α	3.877327 \pm 0.000045	18.7 \pm 5.2	12.47 \pm 0.09	
290	5930.32	Ly α	3.878231 \pm 0.000009	20.1 \pm 0.8	13.64 \pm 0.01	
291	5931.22	Ly α	3.878969 \pm 0.000088	19.9 \pm 11.6	12.58 \pm 0.27	
292	5932.06	Ly α	3.879661 \pm 0.000019	22.4 \pm 1.7	13.43 \pm 0.03	
293	5933.61	Ly α	3.880937 \pm 0.000033	43.0 \pm 2.5	13.55 \pm 0.03	
294	5934.37	Ly α	3.881564 \pm 0.000008	14.4 \pm 0.9	13.32 \pm 0.04	
295	5939.92	Ly α	3.886130 \pm 0.000013	23.1 \pm 1.2	13.22 \pm 0.02	
296	5941.03	Ly α	3.887040 \pm 0.000005	19.9 \pm 0.5	13.73 \pm 0.01	
297	5942.83	Ly α	3.888519 \pm 0.000303	39.1 \pm 7.5	13.56 \pm 0.32	
298	5943.04	Ly α	3.888698 \pm 0.000052	18.6 \pm 5.8	13.33 \pm 0.40	

TABLE 1 — *Continued*

	λ_{obs}	ID	$z \pm \sigma$	$b \pm \sigma$	$\log N \pm \sigma$	Note
299	5943.96	Ly α	3.889450 \pm 0.000045	16.1 \pm 6.2	13.09 \pm 0.31	
300	5944.58	Ly α	3.889959 \pm 0.000018	15.2 \pm 1.2	13.39 \pm 0.04	
301	5945.62	Ly α	3.890814 \pm 0.000007	23.4 \pm 0.6	13.52 \pm 0.01	
302	5948.26	Ly α	3.892985 \pm 0.000003	27.5 \pm 0.4	14.81 \pm 0.04	
303	5951.39	Ly α	3.895561 \pm 0.000047	20.2 \pm 4.2	12.46 \pm 0.07	
304	5952.75	Ly α	3.896685 \pm 0.000006	21.9 \pm 0.5	13.55 \pm 0.01	
305	5954.41	Ly α	3.898048 \pm 0.000007	23.5 \pm 0.6	13.59 \pm 0.01	
306	5955.30	SiIII 1206	3.936010 \pm 0.000005	5.5 \pm 0.6	12.19 \pm 0.03	
307	5955.89	SiIII 1206	3.936501 \pm 0.000006	5.3 \pm 0.8	12.07 \pm 0.05	
308	5956.62	Ly α	3.899869 \pm 0.000046	44.0 \pm 4.2	13.13 \pm 0.04	
309	5958.72	Ly α	3.901596 \pm 0.000026	21.6 \pm 2.5	12.74 \pm 0.04	
310	5959.51	Ly α	3.902242 \pm 0.000020	9.2 \pm 2.3	12.48 \pm 0.13	
311	5960.44	Ly α	3.903008 \pm 0.000010	35.7 \pm 1.2	13.89 \pm 0.01	
312	5962.12	Ly α	3.904392 \pm 0.000006	21.3 \pm 0.6	13.90 \pm 0.01	
313	5963.26	Ly α	3.905324 \pm 0.000028	18.1 \pm 2.7	12.78 \pm 0.05	
314	5966.25	Ly α	3.907790 \pm 0.000066	15.1 \pm 3.7	12.77 \pm 0.18	
315	5966.98	Ly α	3.908387 \pm 0.000020	23.7 \pm 1.3	13.73 \pm 0.02	
316	5968.70	Ly α	3.909805 \pm 0.000010	20.9 \pm 0.9	14.30 \pm 0.04	
317	5970.10	Ly α	3.910958 \pm 0.000011	25.6 \pm 1.7	14.26 \pm 0.04	
318	5971.23	Ly α	3.911883 \pm 0.000059	18.1 \pm 5.2	12.88 \pm 0.16	
319	5972.40	Ly α	3.912848 \pm 0.000073	43.6 \pm 7.0	13.16 \pm 0.06	
320	5974.81	Ly α	3.914829 \pm 0.000016	16.3 \pm 1.7	13.58 \pm 0.07	
321	5975.04	Ly α	3.915016 \pm 0.000032	41.2 \pm 2.9	13.77 \pm 0.04	
322	5977.45	Ly α	3.917003 \pm 0.000014	29.9 \pm 1.6	15.15 \pm 0.11	
323	5979.12	Ly α	3.918378 \pm 0.000121	57.0 \pm 15.7	13.84 \pm 0.12	
324	5980.68	Ly α	3.919659 \pm 0.000050	24.1 \pm 7.4	13.01 \pm 0.25	
325	5981.74	Ly α	3.920531 \pm 0.000021	22.2 \pm 2.6	13.37 \pm 0.05	
326	5983.06	Ly α	3.921614 \pm 0.000292	28.5 \pm 14.1	13.43 \pm 0.36	
327	5983.74	Ly α	3.922178 \pm 0.000025	17.3 \pm 3.6	14.30 \pm 0.12	
328	5984.60	Ly α	3.922879 \pm 0.000041	24.5 \pm 1.9	13.85 \pm 0.05	
329	5987.28	Ly α	3.925089 \pm 0.000006	38.1 \pm 0.9	15.10 \pm 0.05	
330	5989.24	Ly α	3.926695 \pm 0.000020	6.3 \pm 2.3	12.23 \pm 0.10	
331	5990.83	Ly α	3.928009 \pm 0.000008	29.9 \pm 0.6	13.82 \pm 0.01	
332	5994.19	Ly α	3.930769 \pm 0.000038	25.0 \pm 3.8	12.82 \pm 0.07	
333	5995.43	Ly α	3.931789 \pm 0.000046	15.6 \pm 4.9	12.47 \pm 0.15	
334	5997.55	Ly α (M)	3.933534 \pm 0.003220	30.6 \pm 33.1	15.09 \pm 7.36	1
335	5999.89	Ly α (M)	3.935460 \pm 0.000142	51.1 \pm 3.1	18.43 \pm 0.06	1
336	6004.23	Ly α	3.939033 \pm 0.000042	17.1 \pm 5.4	12.57 \pm 0.17	
337	6006.30	Ly α	3.940730 \pm 0.000025	20.4 \pm 1.0	14.09 \pm 0.06	
338	6007.46	Ly α	3.941687 \pm 0.000032	36.7 \pm 2.4	14.24 \pm 0.03	
339	6009.61	Ly α	3.943454 \pm 0.000008	30.7 \pm 0.8	14.68 \pm 0.04	
340	6012.97	Ly α	3.946222 \pm 0.000042	25.9 \pm 2.2	13.53 \pm 0.05	
341	6013.85	Ly α	3.946945 \pm 0.000017	22.0 \pm 0.9	13.94 \pm 0.03	
342	6015.86	Ly α	3.948600 \pm 0.000018	9.8 \pm 1.7	13.08 \pm 0.07	
343	6016.34	Ly α	3.948988 \pm 0.000013	50.6 \pm 0.9	13.96 \pm 0.01	
344	6019.02	Ly α	3.951195 \pm 0.000008	25.8 \pm 0.8	13.49 \pm 0.01	
345	6020.42	Ly α	3.952348 \pm 0.000063	17.3 \pm 2.3	13.43 \pm 0.15	
346	6021.09	Ly α	3.952896 \pm 0.000019	17.5 \pm 1.9	14.40 \pm 0.09	
347	6022.37	Ly α	3.953954 \pm 0.000015	38.0 \pm 2.1	13.99 \pm 0.02	
348	6023.94	Ly α	3.955241 \pm 0.000064	30.2 \pm 7.4	12.92 \pm 0.11	

TABLE 1 — *Continued*

	λ_{obs}	ID	$z \pm \sigma$	$b \pm \sigma$	$\log N \pm \sigma$	Note
349	6025.03	Ly α	3.956142 \pm 0.000008	16.8 \pm 0.7	13.43 \pm 0.02	
350	6026.33	Ly α	3.957212 \pm 0.000007	36.2 \pm 0.6	14.05 \pm 0.01	
351	6029.77	Ly α	3.960035 \pm 0.000019	74.6 \pm 3.8	13.73 \pm 0.02	
352	6029.81	Ly α	3.960071 \pm 0.000004	19.8 \pm 0.7	14.24 \pm 0.04	
353	6032.17	Ly α	3.962012 \pm 0.000025	19.0 \pm 2.4	12.75 \pm 0.07	
354	6034.10	Ly α	3.963602 \pm 0.000027	63.2 \pm 1.9	13.87 \pm 0.01	
355	6034.63	Ly α	3.964037 \pm 0.000012	23.4 \pm 1.3	13.52 \pm 0.04	
356	6039.70	Ly α	3.968204 \pm 0.000015	17.7 \pm 0.3	17.93 \pm 0.01	
357	6040.65	Ly α	3.968985 \pm 0.000276	43.7 \pm 9.6	14.01 \pm 0.23	
358	6043.65	Ly α	3.971455 \pm 0.000010	25.1 \pm 1.8	14.41 \pm 0.05	
359	6044.05	Ly α	3.971787 \pm 0.000168	68.4 \pm 15.0	13.97 \pm 0.04	
360	6046.15	Ly α	3.973511 \pm 0.000031	36.4 \pm 3.8	13.78 \pm 0.08	
361	6047.09	Ly α	3.974284 \pm 0.000033	15.0 \pm 3.7	12.65 \pm 0.21	
362	6050.71	Ly α	3.977263 \pm 0.000023	27.1 \pm 1.6	13.16 \pm 0.03	
363	6051.72	Ly α	3.978091 \pm 0.000008	21.8 \pm 0.6	13.48 \pm 0.01	
364	6053.78	Ly α	3.979787 \pm 0.000063	48.6 \pm 5.9	12.70 \pm 0.04	
365	6057.21	Ly α	3.982614 \pm 0.000055	21.3 \pm 2.6	13.05 \pm 0.09	
366	6057.81	Ly α	3.983105 \pm 0.000027	16.7 \pm 2.0	13.08 \pm 0.09	
367	6059.34	Ly α	3.984362 \pm 0.000004	28.9 \pm 0.7	14.64 \pm 0.03	
368	6061.35	Ly α	3.986019 \pm 0.000012	35.9 \pm 1.1	13.99 \pm 0.01	
369	6062.65	Ly α	3.987081 \pm 0.000012	23.4 \pm 0.8	13.74 \pm 0.02	
370	6064.46	Ly α	3.988575 \pm 0.000015	21.7 \pm 0.8	14.02 \pm 0.02	
371	6065.24	Ly α	3.989216 \pm 0.000015	15.6 \pm 0.9	13.70 \pm 0.03	
372	6067.39	Ly α	3.990981 \pm 0.000016	9.0 \pm 0.4	17.25 \pm 0.09	
373	6067.76	Ly α	3.991291 \pm 0.000042	35.5 \pm 1.7	14.02 \pm 0.06	
374	6070.40	Ly α	3.993458 \pm 0.000028	45.6 \pm 3.1	13.35 \pm 0.02	
375	6072.39	Ly α	3.995096 \pm 0.000004	22.2 \pm 0.6	15.47 \pm 0.10	
376	6074.55	Ly α	3.996874 \pm 0.000427	33.9 \pm 13.7	13.43 \pm 0.44	
377	6074.82	Ly α	3.997100 \pm 0.000022	14.1 \pm 3.0	13.52 \pm 0.24	
378	6076.13	Ly α	3.998173 \pm 0.000019	25.1 \pm 2.1	14.74 \pm 0.09	
379	6077.59	Ly α	3.999375 \pm 0.000057	38.5 \pm 6.3	13.56 \pm 0.07	
380	6078.90	Ly α	4.000455 \pm 0.000026	18.3 \pm 1.9	13.54 \pm 0.08	
381	6081.00	Ly α	4.002181 \pm 0.000017	47.6 \pm 3.1	15.39 \pm 0.12	
382	6083.44	Ly α	4.004184 \pm 0.000038	26.6 \pm 2.0	13.34 \pm 0.05	
383	6085.79	Ly α	4.006120 \pm 0.000020	28.9 \pm 1.7	13.21 \pm 0.02	
384	6088.48	Ly α	4.008336 \pm 0.000007	49.8 \pm 1.1	14.84 \pm 0.03	
385	6091.24	Ly α	4.010607 \pm 0.000034	38.9 \pm 3.9	13.21 \pm 0.04	
386	6093.37	Ly α	4.012354 \pm 0.000019	39.8 \pm 2.2	13.59 \pm 0.02	
387	6094.56	Ly α	4.013335 \pm 0.000013	17.8 \pm 1.2	13.20 \pm 0.04	
388	6096.20	Ly α	4.014680 \pm 0.000034	47.9 \pm 3.7	13.22 \pm 0.03	
389	6098.01	Ly α	4.016174 \pm 0.000041	18.1 \pm 2.9	12.85 \pm 0.10	
390	6098.85	Ly α	4.016860 \pm 0.000027	25.7 \pm 2.0	13.33 \pm 0.03	
391	6100.50	Ly α	4.018223 \pm 0.000075	20.9 \pm 3.8	13.02 \pm 0.12	
392	6101.43	Ly α	4.018983 \pm 0.000010	21.9 \pm 1.5	14.16 \pm 0.03	
393	6102.52	Ly α	4.019881 \pm 0.000034	22.3 \pm 4.7	13.20 \pm 0.09	
394	6103.47	Ly α	4.020663 \pm 0.000023	19.6 \pm 1.9	13.23 \pm 0.04	
395	6104.82	Ly α	4.021771 \pm 0.000014	25.9 \pm 1.5	13.31 \pm 0.02	
396	6105.75	SiIII 1206	4.060716 \pm 0.000006	7.2 \pm 0.6	12.37 \pm 0.03	
397	6106.69	Ly α	4.023312 \pm 0.000007	19.8 \pm 0.6	13.80 \pm 0.01	
398	6108.71	Ly α	4.024972 \pm 0.000143	55.3 \pm 6.0	14.14 \pm 0.09	

TABLE 1 — *Continued*

	λ_{obs}	ID	$z \pm \sigma$	$b \pm \sigma$	$\log N \pm \sigma$	Note
399	6109.61	Ly α	4.025710 \pm 0.000018	24.0 \pm 2.4	14.71 \pm 0.11	
400	6111.48	Ly α	4.027252 \pm 0.000014	25.4 \pm 1.0	13.55 \pm 0.02	
401	6114.59	Ly α	4.029807 \pm 0.000027	27.6 \pm 2.4	12.92 \pm 0.03	
402	6115.96	SiIV 1393	3.388119 \pm 0.000005	13.6 \pm 0.3	13.31 \pm 0.02	
403	6116.09	SiIV 1393	3.388208 \pm 0.000003	2.9 \pm 0.6	12.93 \pm 0.04	
404	6116.79	SiIV 1393	3.388710 \pm 0.000003	2.8 \pm 0.5	12.86 \pm 0.04	
405	6117.14	SiIV 1393	3.388967 \pm 0.000008	20.5 \pm 0.6	13.35 \pm 0.01	
406	6118.17	SiIV 1393	3.389699 \pm 0.000002	4.6 \pm 0.2	13.17 \pm 0.02	
407	6118.49	SiIV 1393	3.389934 \pm 0.000007	3.8 \pm 0.7	12.92 \pm 0.09	
408	6118.75	SiIV 1393	3.390116 \pm 0.000009	8.7 \pm 1.5	13.27 \pm 0.08	
409	6119.24	SiIV 1393	3.390471 \pm 0.000005	2.9 \pm 1.2	12.80 \pm 0.08	
410	6119.38	Ly α	4.033751 \pm 0.000025	28.5 \pm 2.2	14.35 \pm 0.05	
411	6119.54	SiIV 1393	3.390689 \pm 0.000005	2.4 \pm 1.1	12.82 \pm 0.07	
412	6119.98	SiIV 1393	3.391001 \pm 0.000005	1.1 \pm 1.2	12.82 \pm 0.50	
413	6120.27	SiIV 1393	3.391209 \pm 0.000003	6.4 \pm 0.5	13.32 \pm 0.03	
414	6120.63	SiIV 1393	3.391467 \pm 0.000025	15.1 \pm 1.7	12.99 \pm 0.06	
415	6123.67	Ly α	4.037282 \pm 0.000023	53.3 \pm 2.2	13.26 \pm 0.01	
416	6126.93	Ly α	4.039963 \pm 0.000016	10.2 \pm 2.0	12.62 \pm 0.11	
417	6127.42	Ly α	4.040368 \pm 0.000025	66.4 \pm 2.4	13.73 \pm 0.03	
418	6128.02	Ly α	4.040855 \pm 0.000004	18.6 \pm 0.5	14.50 \pm 0.04	
419	6131.03	Ly α	4.043334 \pm 0.000007	29.4 \pm 0.6	13.38 \pm 0.01	
420	6137.14	Ly α	4.048357 \pm 0.000064	22.3 \pm 5.7	12.14 \pm 0.09	
421	6138.66	Ly α	4.049610 \pm 0.000026	21.1 \pm 2.3	12.71 \pm 0.04	
422	6139.46	Ly α	4.050270 \pm 0.000016	14.7 \pm 1.4	12.68 \pm 0.04	
423	6142.36	Ly α	4.052653 \pm 0.000027	27.2 \pm 3.4	12.75 \pm 0.09	
424	6143.01	Ly α	4.053187 \pm 0.000172	93.3 \pm 13.7	13.10 \pm 0.03	
425	6145.31	Ly α	4.055079 \pm 0.000016	23.7 \pm 1.9	12.88 \pm 0.05	
426	6146.73	Ly α	4.056249 \pm 0.000007	27.1 \pm 0.7	13.39 \pm 0.01	
427	6148.21	Ly α	4.057467 \pm 0.000019	24.1 \pm 1.1	13.37 \pm 0.05	
428	6148.78	Ly α	4.057932 \pm 0.000040	29.9 \pm 1.9	13.27 \pm 0.06	
429	6152.48	Ly α (M)	4.060977 \pm 0.000010	22.0 \pm 0.6	17.17 \pm 0.18	1
430	6152.79	Ly α (M)	4.061234 \pm 0.000007	67.3 \pm 0.9	14.60 \pm 0.01	1
431	6155.52	SiIV 1402	3.388119 \pm 0.000005	13.6 \pm 0.3	13.31 \pm 0.02	
432	6155.65	SiIV 1402	3.388208 \pm 0.000003	2.9 \pm 0.6	12.93 \pm 0.04	
433	6156.35	SiIV 1402	3.388710 \pm 0.000003	2.8 \pm 0.5	12.86 \pm 0.04	
434	6156.41	Ly α	4.064214 \pm 0.000009	30.5 \pm 0.9	13.51 \pm 0.01	
435	6156.71	SiIV 1402	3.388967 \pm 0.000008	20.5 \pm 0.6	13.35 \pm 0.01	
436	6157.74	SiIV 1402	3.389699 \pm 0.000002	4.6 \pm 0.2	13.17 \pm 0.02	
437	6158.07	SiIV 1402	3.389934 \pm 0.000007	3.8 \pm 0.7	12.92 \pm 0.09	
438	6158.32	SiIV 1402	3.390116 \pm 0.000009	8.7 \pm 1.5	13.27 \pm 0.08	
439	6158.82	SiIV 1402	3.390471 \pm 0.000005	2.9 \pm 1.2	12.80 \pm 0.08	
440	6159.10	Ly α	4.066425 \pm 0.000035	40.6 \pm 2.7	13.85 \pm 0.03	
441	6159.13	SiIV 1402	3.390689 \pm 0.000005	2.4 \pm 1.1	12.82 \pm 0.07	
442	6159.56	SiIV 1402	3.391001 \pm 0.000005	1.1 \pm 1.2	12.82 \pm 0.50	
443	6159.86	SiIV 1402	3.391209 \pm 0.000003	6.4 \pm 0.5	13.32 \pm 0.03	
444	6160.22	SiIV 1402	3.391467 \pm 0.000025	15.1 \pm 1.7	12.99 \pm 0.06	
445	6160.56	Ly α	4.067622 \pm 0.000016	13.9 \pm 1.8	12.87 \pm 0.07	
446	6161.94	Ly α	4.068764 \pm 0.000003	25.5 \pm 0.3	15.14 \pm 0.03	
447	6166.66	Ly α	4.072639 \pm 0.000020	30.1 \pm 1.8	12.98 \pm 0.02	
448	6168.24	Ly α	4.073944 \pm 0.000013	23.3 \pm 0.7	13.81 \pm 0.02	

TABLE 1 — *Continued*

λ_{obs}	ID	$z \pm \sigma$	$b \pm \sigma$	$\log N \pm \sigma$	Note	
449	6169.09	Ly α	4.074638 \pm 0.000065	27.9 \pm 3.2	13.22 \pm 0.08	
450	6170.76	Ly α	4.076012 \pm 0.000018	19.5 \pm 1.6	12.73 \pm 0.03	
451	6172.24	Ly α	4.077235 \pm 0.000016	24.2 \pm 1.4	12.88 \pm 0.02	
452	6174.13	Ly α	4.078790 \pm 0.000012	19.6 \pm 1.1	12.87 \pm 0.02	
453	6175.45	Ly α	4.079875 \pm 0.000004	20.0 \pm 0.4	13.45 \pm 0.01	
454	6176.96	Ly α	4.081117 \pm 0.000016	25.2 \pm 1.5	12.93 \pm 0.02	
455	6178.60	Ly α	4.082462 \pm 0.000376	22.9 \pm 14.5	12.48 \pm 0.62	
456	6179.21	Ly α	4.082966 \pm 0.000039	21.0 \pm 1.5	13.37 \pm 0.08	
457	6180.96	SiIV 1393	3.434754 \pm 0.000020	17.4 \pm 1.8	12.65 \pm 0.05	
458	6181.34	SiIV 1393	3.435029 \pm 0.000005	2.2 \pm 1.0	12.27 \pm 0.05	
459	6181.97	Ly α	4.085238 \pm 0.000013	30.6 \pm 1.1	13.42 \pm 0.01	
460	6184.15	Ly α	4.087030 \pm 0.000015	22.2 \pm 1.3	13.01 \pm 0.03	
461	6186.44	Ly α	4.088911 \pm 0.000005	31.0 \pm 1.0	14.96 \pm 0.05	
462	6187.11	Ly α	4.089462 \pm 0.000090	68.4 \pm 2.3	13.89 \pm 0.06	
463	6190.31	Ly α	4.092094 \pm 0.000015	28.4 \pm 0.5	13.87 \pm 0.02	
464	6190.71	Ly α	4.092422 \pm 0.000014	13.1 \pm 1.5	13.20 \pm 0.09	
465	6192.24	Ly α	4.093685 \pm 0.000022	30.3 \pm 2.6	12.97 \pm 0.03	
466	6193.35	SiIII 1206	4.133322 \pm 0.000028	15.4 \pm 2.7	12.14 \pm 0.07	
467	6193.69	SiIII 1206	4.133601 \pm 0.000005	4.0 \pm 0.8	12.03 \pm 0.07	
468	6194.04	SiIII 1206	4.133893 \pm 0.000017	10.2 \pm 2.2	12.04 \pm 0.10	
469	6194.57	SiIII 1206	4.134328 \pm 0.000019	17.2 \pm 1.3	12.48 \pm 0.03	
470	6196.22	Ly α	4.096956 \pm 0.000003	25.1 \pm 0.2	13.78 \pm 0.00	
471	6199.76	Ly α	4.099868 \pm 0.000014	23.1 \pm 1.0	13.18 \pm 0.02	
472	6201.14	Ly α	4.101006 \pm 0.000004	27.9 \pm 0.4	14.40 \pm 0.01	
473	6203.71	Ly α	4.103117 \pm 0.000048	40.2 \pm 4.8	12.60 \pm 0.04	
474	6208.85	Ly α	4.107350 \pm 0.000036	37.5 \pm 3.0	12.99 \pm 0.03	
475	6210.63	Ly α	4.108816 \pm 0.000020	18.7 \pm 2.5	12.86 \pm 0.11	
476	6210.87	Ly α	4.109009 \pm 0.000052	43.6 \pm 2.7	13.24 \pm 0.05	
477	6215.95	Ly α	4.113187 \pm 0.000041	44.8 \pm 3.8	12.91 \pm 0.03	
478	6217.55	Ly α	4.114505 \pm 0.000023	19.6 \pm 1.9	12.87 \pm 0.05	
479	6218.65	Ly α	4.115408 \pm 0.000005	26.3 \pm 0.4	13.95 \pm 0.01	
480	6220.94	SiIV 1402	3.434754 \pm 0.000020	17.4 \pm 1.8	12.65 \pm 0.05	
481	6221.22	Ly α	4.117524 \pm 0.000017	31.8 \pm 1.7	13.09 \pm 0.02	
482	6221.33	SiIV 1402	3.435029 \pm 0.000005	2.2 \pm 1.0	12.27 \pm 0.05	
483	6222.31	Ly α	4.118421 \pm 0.000034	9.7 \pm 3.5	11.95 \pm 0.13	
484	6225.87	Ly α	4.121351 \pm 0.000052	29.8 \pm 4.4	12.38 \pm 0.05	
485	6231.12	Ly α	4.125664 \pm 0.000164	36.8 \pm 4.3	13.56 \pm 0.17	
486	6231.53	Ly α	4.126003 \pm 0.000009	21.2 \pm 2.5	13.42 \pm 0.20	
487	6232.57	Ly α	4.126858 \pm 0.000070	31.0 \pm 2.7	13.09 \pm 0.09	
488	6236.62	Ly α (M)	4.130191 \pm 0.000074	28.5 \pm 0.5	16.72 \pm 0.40	1
489	6240.21	Ly α (M)	4.133141 \pm 0.000065	44.9 \pm 0.9	17.28 \pm 0.15	1
λ_{obs}	$W_{obs} \pm \sigma$	ID	z	Note		
490	6259.37	0.090 \pm 0.015			7	
491	6273.14	0.187 \pm 0.017	CIV 1548	3.0519		
492	6276.40	0.050 \pm 0.009				
493	6283.33	0.071 \pm 0.012	CIV 1550	3.0517		
494	6295.55	0.022 \pm 0.007	FeII 2586	1.4339	8	
495	6296.42	0.057 \pm 0.006	FeII 2586	1.4342	9	
496	6321.63	0.109 \pm 0.017	SiIV 1393	3.5357		

TABLE 1 — *Continued*

	λ_{obs}	$W_{obs} \pm \sigma$	ID	z	Note
497	6323.26	0.158± 0.021	SiIV 1393	3.5369	
498	6328.39	0.063± 0.007	FeII 2600	1.4338	
499	6329.30	0.130± 0.008	FeII 2600	1.4342	
500	6354.75	0.028± 0.006	NV 1238	4.1297	
501	6356.36	0.119± 0.012	NV 1238	4.1310	
502	6358.15	0.134± 0.012	NV 1238	4.1324	
503	6360.28	0.274± 0.025	NV 1238	4.1341	
504	6362.51	0.057± 0.010	SiIV 1402	3.5357	
505	6364.25	0.068± 0.011	SiIV 1402	3.5369	
506	6376.65	0.045± 0.008	NV 1242	4.1309	
507	6378.56	0.068± 0.013	NV 1242	4.1324	
508	6380.90	0.134± 0.024	NV 1242	4.1343	
509	6406.63	0.101± 0.026			
510	6442.35	0.158± 0.031	CIV 1548	3.1612	10
511	6443.55	0.142± 0.031	CIV 1548	3.1620	10
512	6513.70	0.071± 0.014	SiIV 1393	3.6735	
513	6575.54	0.092± 0.025			
514	6617.01	0.262± 0.020	SiIV 1393	3.7476	
515	6659.88	0.159± 0.036	SiIV 1402	3.7477	
516	6702.36	1.438± 0.034	SiII 1526	3.3901	
517	6713.41	0.041± 0.008	CIV 1548	3.3363	
518	6716.50	0.166± 0.013	SiIV 1393	3.8190	
519	6724.49	0.031± 0.006	CIV 1550	3.3362	
520	6759.94	0.100± 0.016	SiIV 1402	3.8190	
521	6796.35	4.247± 0.084	CIV 1548	3.3899	
522	6802.53	0.150± 0.013	MgII 2796	1.4326	
523	6807.43	3.569± 0.084	CIV 1550	3.3897	
			MgII 2796	1.4344	
524	6819.88	0.143± 0.023	MgII 2803	1.4326	
525	6822.52	0.175± 0.020	MgII 2803	1.4335	
526	6823.34	0.241± 0.016	MgII 2803	1.4338	
527	6824.34	0.348± 0.014	MgII 2803	1.4342	
528	6853.47	0.045± 0.011			
529	6860.00	0.048± 0.009			
530	6866.02	0.719± 0.032	CIV 1548	3.4349	7
531	6877.44	0.000± 0.000	CIV 1550	3.4349	9
532	6879.57	0.117± 0.009	SiIV 1393	3.9360	9
533	6880.34	0.209± 0.010	SiIV 1393	3.9365	9
534	6924.05	0.073± 0.018	SiIV 1402	3.9360	
535	6924.70	0.123± 0.022	SiIV 1402	3.9364	9
536	6980.60	0.081± 0.020			
537	7007.66	0.069± 0.014			
538	7022.24	0.401± 0.030	CIV 1548	3.5358	
539	7024.01	0.421± 0.030	CIV 1548	3.5369	
540	7033.94	0.217± 0.033	CIV 1550	3.5358	
541	7035.72	0.258± 0.036	CIV 1550	3.5369	
542	7053.40	0.107± 0.013	SiIV 1393	4.0607	
543	7056.54	0.319± 0.058			
544	7060.31	0.099± 0.023	FeII 1608	3.3895	
545	7061.18	0.681± 0.021	FeII 1608	3.3900	

TABLE 1 — *Continued*

	λ_{obs}	$W_{obs} \pm \sigma$	ID	z	Note
546	7094.87	0.069± 0.016			
547	7110.05	0.157± 0.020	CIV 1548	3.5925	
548	7113.01	0.353± 0.041	CIV 1548	3.5944	
549	7114.70	0.049± 0.009			
550	7121.94	0.058± 0.017	CIV 1550	3.5925	8
551	7124.96	0.163± 0.023	CIV 1550	3.5945	
552	7144.42	0.037± 0.009			
553	7151.43	0.152± 0.016	SiIV 1393	4.1311	
554	7153.18	0.118± 0.024	SiIV 1393	4.1323	
555	7155.41	0.461± 0.053	SiIV 1393	4.1339	
556	7159.79	0.088± 0.020	CIV 1548	3.6246	
557	7171.71	0.055± 0.018	CIV 1550	3.6246	8
558	7201.90	0.305± 0.059	SiIV 1402	4.1340	
559	7235.65	0.303± 0.030	CIV 1548	3.6736	9
560	7247.55	0.150± 0.014	CIV 1550	3.6735	
561	7320.08	0.153± 0.030	CIV 1548	3.7281	
562	7332.49	0.106± 0.029	CIV 1550	3.7283	8
563	7334.76	1.135± 0.041	AlII 1670	3.3900	
564	7336.65	0.117± 0.032	AlII 1670	3.3911	8
565	7349.98	0.316± 0.057	CIV 1548	3.7475	
566	7362.47	0.138± 0.028	CIV 1550	3.7476	
567	7427.56	0.092± 0.018	CIV 1548	3.7976	
568	7439.90	0.035± 0.009	CIV 1550	3.7976	8
569	7460.72	0.216± 0.036	CIV 1548	3.8190	
570	7473.30	0.062± 0.017	CIV 1550	3.8191	8

Notes to Table 1:

- (1) This Ly α line is associated with identified metal systems.
- (2) This feature agrees with the expected position of S II λ 1253 in the $z_{abs} = 3.39$ damped Ly α system. The identification is tentative.
- (3) The Si II $\lambda\lambda$ 1260, 1304 lines are fitted simultaneously with the Si II λ 1526 line redward of Ly α emission.
- (4) The Fe II λ 2344 absorption is fitted simultaneously with the Fe II $\lambda\lambda$ 2586, 2600 absorption redward of Ly α emission.
- (5) The O I λ 1302 absorption is fitted with the redshift and the Doppler width fixed to those of the corresponding Si II components in the same system, hence there are no error estimates for the redshifts and Doppler widths. One of the components is rejected by VPFIT as not necessary.
- (6) The C II λ 1334 absorption is badly blended with the strong Ly α absorption corresponding to the $z_{abs} = 3.8190$ C IV system. Only one component of C II is clearly discernible.
- (7) Contaminated by cosmic rays or poorly subtracted night sky lines.
- (8) This feature has a statistical significance above 3σ but less than 4σ .
- (9) Blended with telluric absorption lines.
- (10) The corresponding C IV λ 1550 absorption occurs in a corrupted part of the spectrum caused by an ink mark on the CCD.

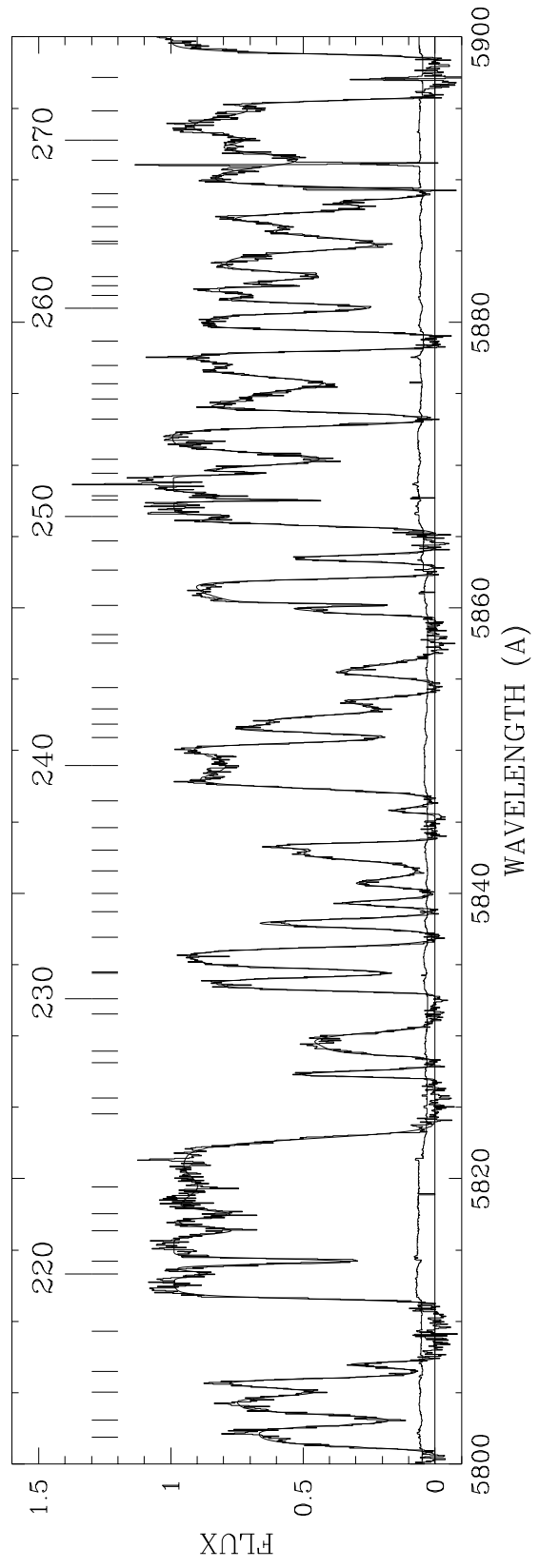
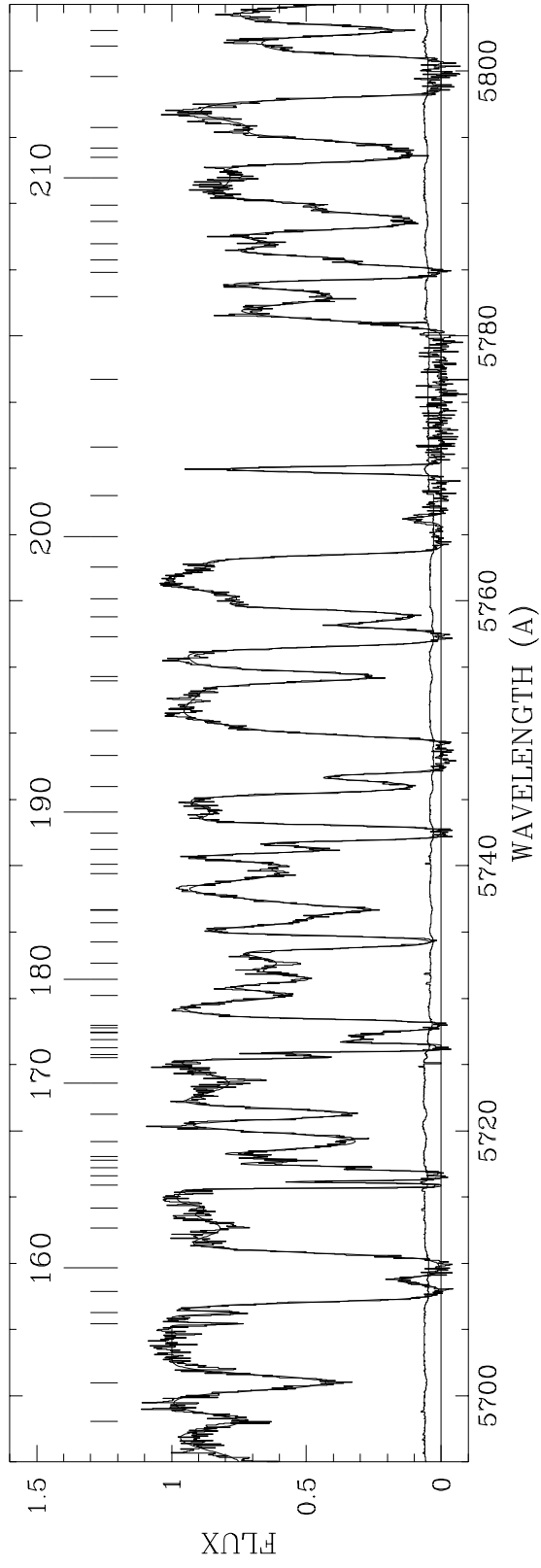


Fig. 2 (sample)

TABLE 2

BEST SIMULATION PARAMETERS^a

A	γ	β	N_{min} (cm^{-2})	N_{max} (cm^{-2})	$\langle b \rangle$ (km s^{-1})	σ (km s^{-1})	b_{cut} (km s^{-1})	b_{max} (km s^{-1})
28.3	2.75 ^b	1.53	2×10^{12}	$10^{18,c}$	23	8	15	100 ^b

Notes to Table 2:

^a The table gives the parameters in eq. (1) of the main text that produce simulated Ly α forest spectra which match the observations satisfactorily.

^b These values are pre-selected. Their exact values have little effects on the simulations.

^c This value is chosen to avoid damped Ly α absorption lines.

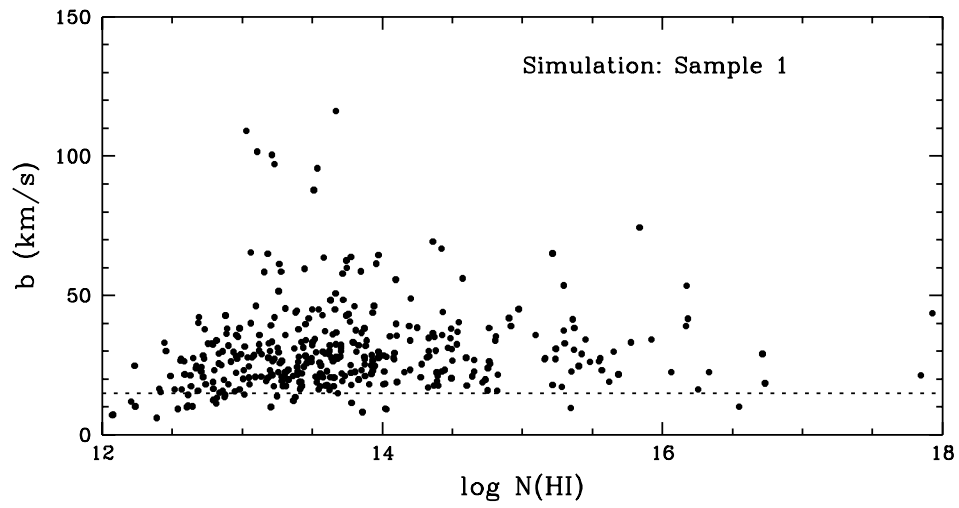
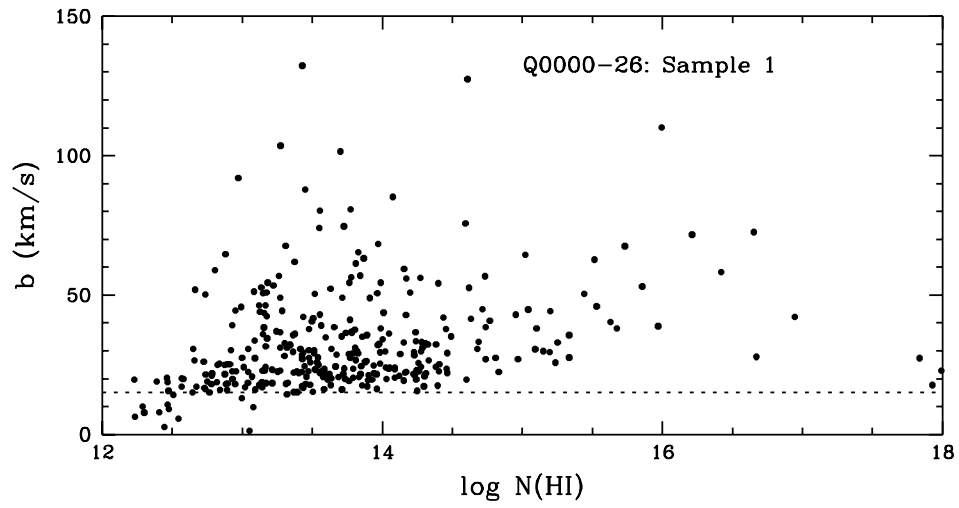


Figure 3

TABLE 3

COLUMN DENSITY DISTRIBUTIONS

Corrected Region ^a	Fit Region ^b	β	Reduced χ^2	Prob ^c
12.3 $<\log N < 13.5$	12.6 $<\log N < 16.0$	1.55 ± 0.05	1.09	0.4
12.3 $<\log N < 13.5$	12.6 $<\log N < 14.5$	1.43 ± 0.07	0.71	0.6
12.3 $<\log N < 13.5$	12.3 $<\log N < 14.5$	1.46 ± 0.06	0.81	0.6
12.3 $<\log N < 13.5$	14.5 $<\log N < 16.0$	1.41 ± 0.18	0.12	1.0
12.3 $<\log N < 16.0$	12.6 $<\log N < 16.0$	1.52 ± 0.06	0.74	0.4
12.3 $<\log N < 16.0$	12.6 $<\log N < 14.5$	1.36 ± 0.10	0.20	0.7
12.3 $<\log N < 16.0$	12.3 $<\log N < 14.5$	1.41 ± 0.09	0.41	0.8
12.3 $<\log N < 16.0$	14.5 $<\log N < 16.0$	1.60 ± 0.32	0.19	0.9

Notes to Table 3:

^a The observed column density distribution in this region is corrected for incompleteness using the simulation results.

^b The corrected, observed column density distribution in this region is fitted to determine the power law index β .

^c Probability for the fit to be acceptable.

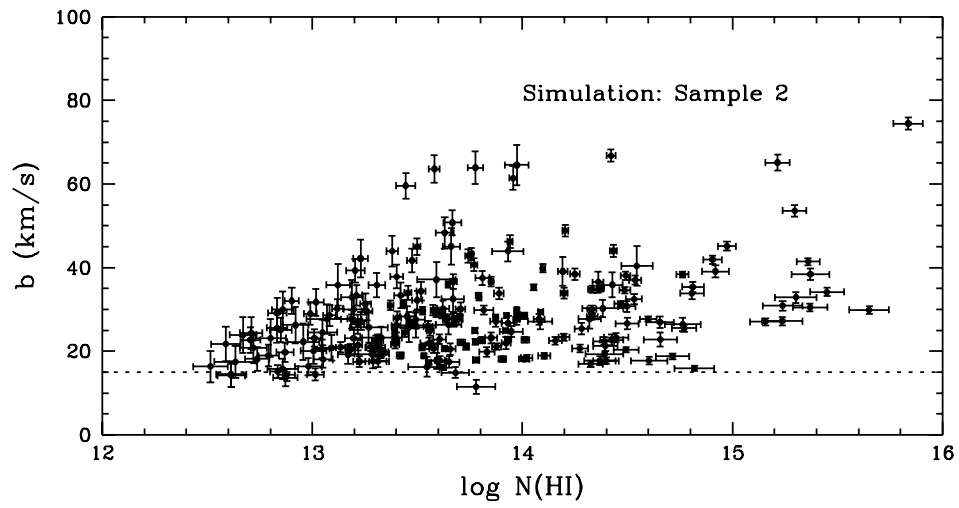
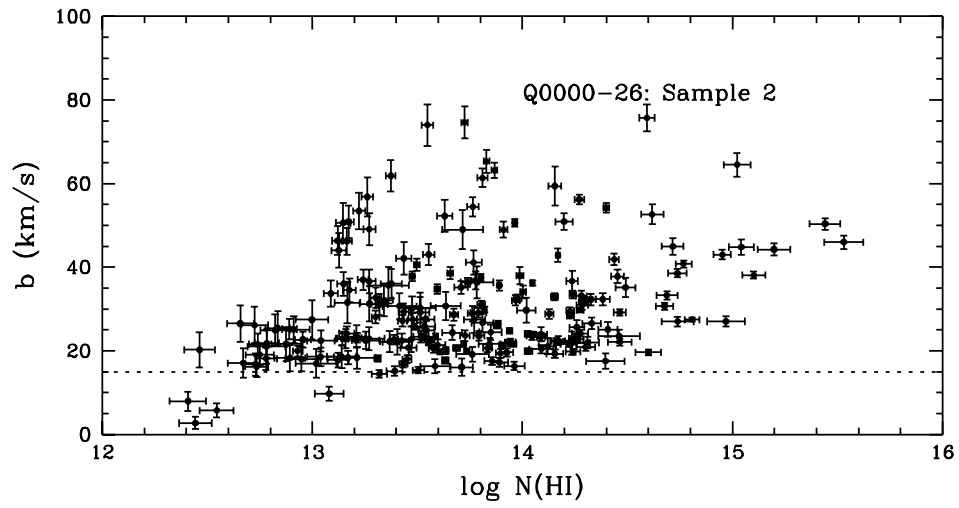


Figure 4

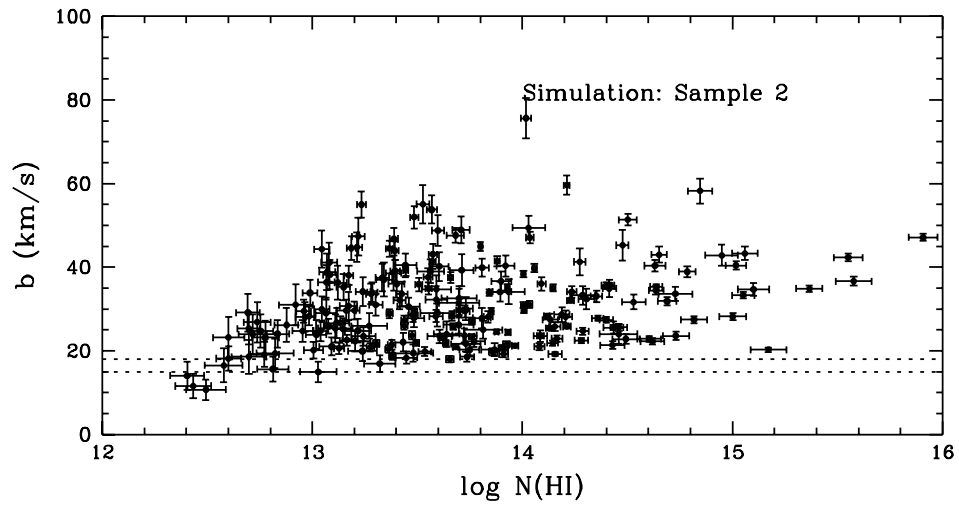


Figure 5

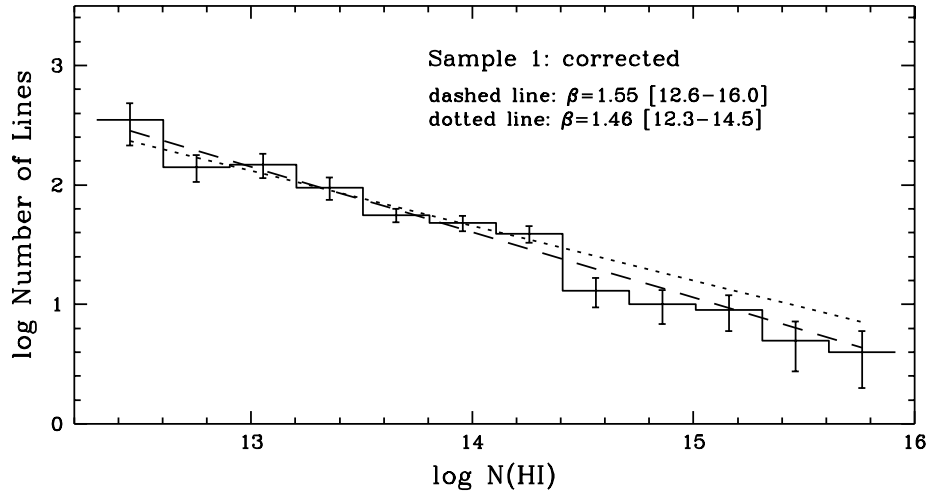
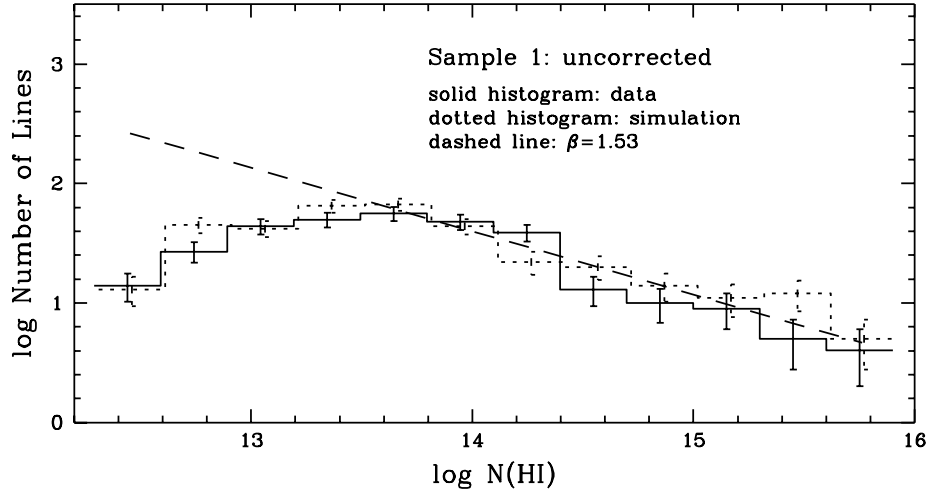


Figure 6

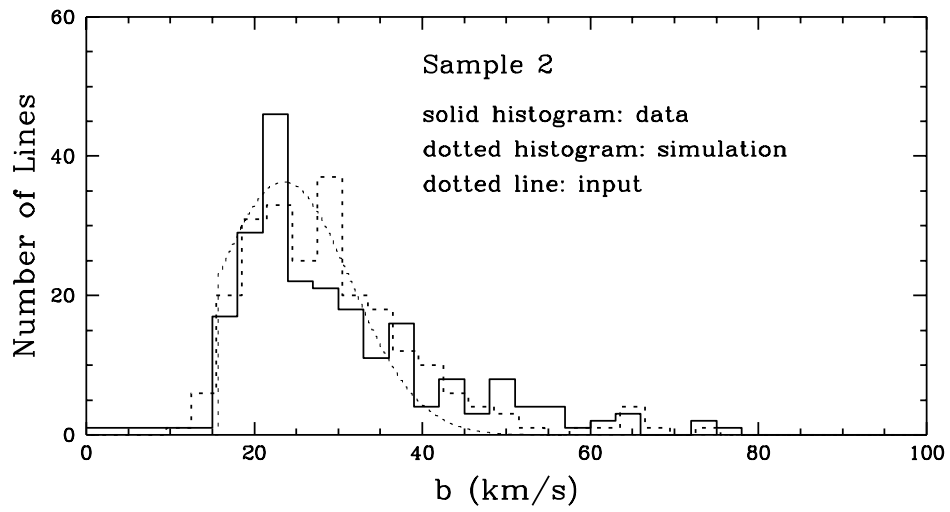
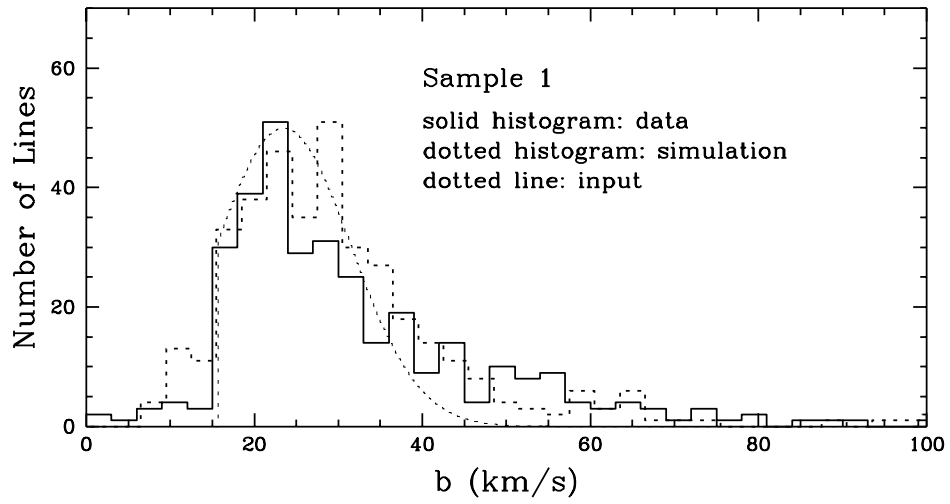
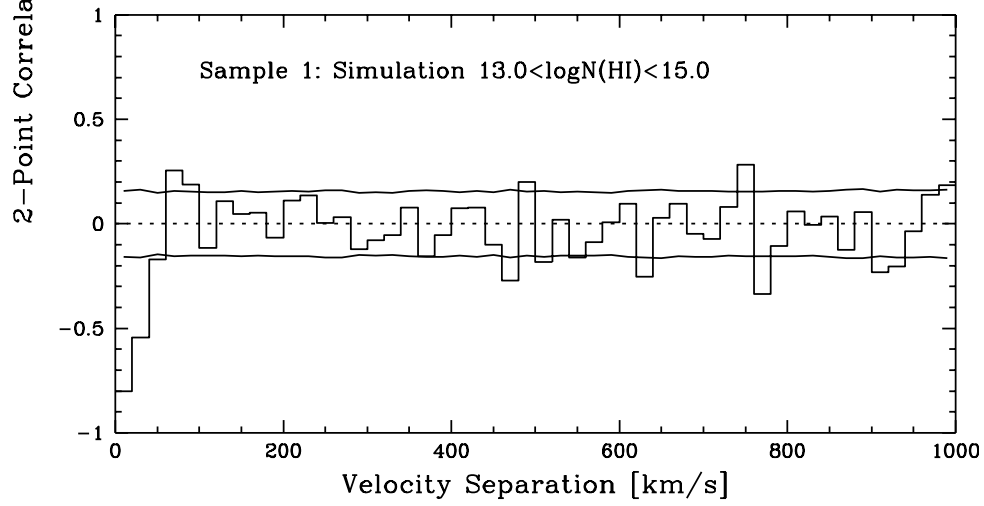
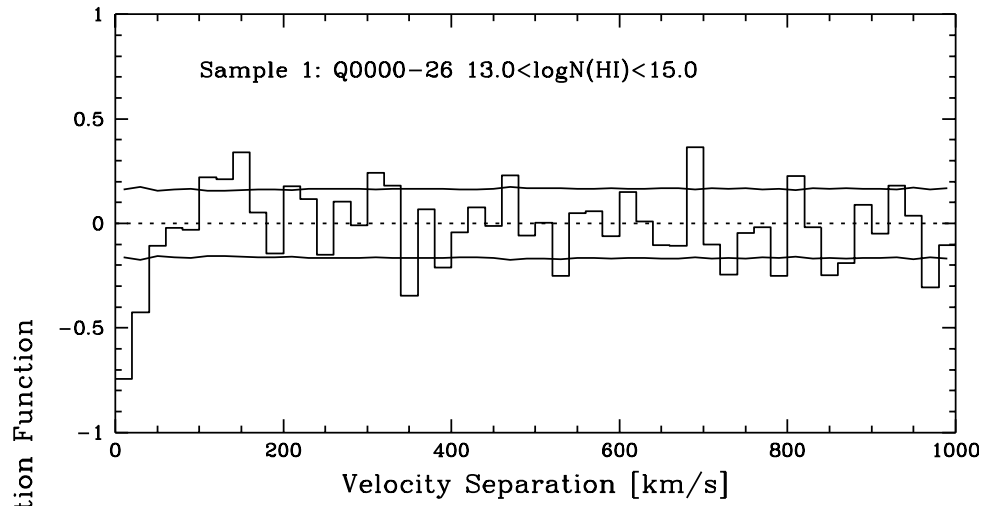


Figure 7



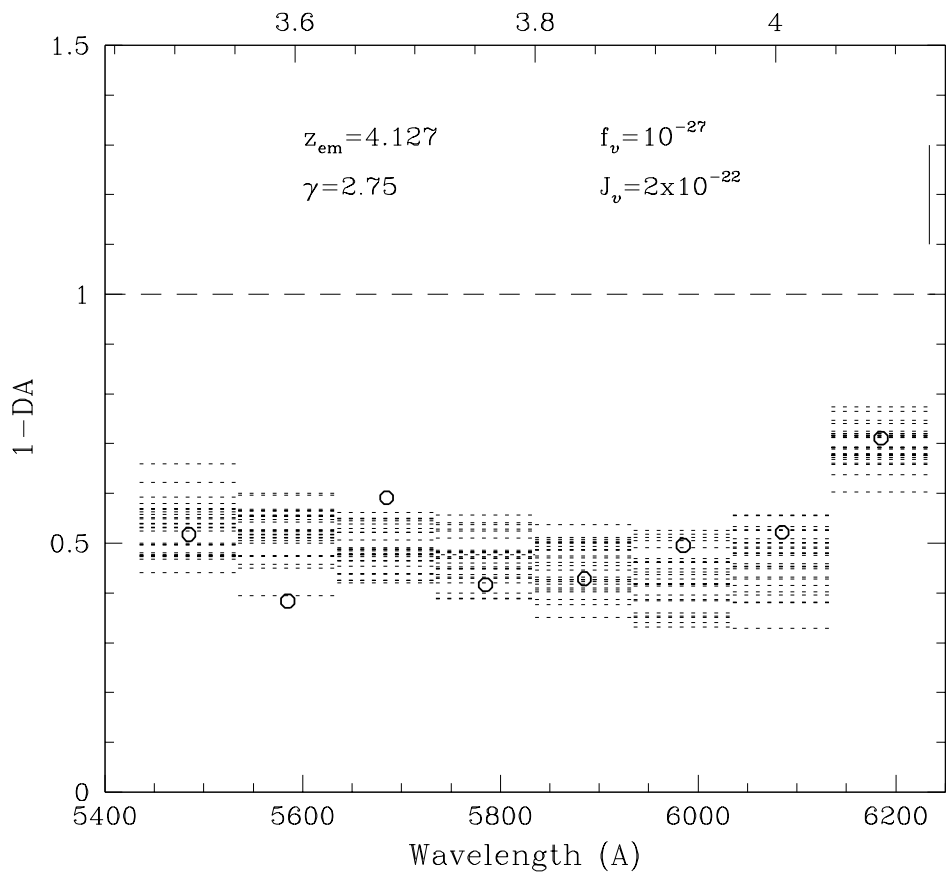


Figure 9